Universiteit Antwerpen

This item is the archived peer-reviewed author-version of:

Measurement of atomic electric fields and charge densities from average momentum transfers using scanning transmission electron microscopy

Reference:

Measurement of atomic electric fields and charge densities from average momentum transfers using scanning transmission electron microscopy

Knut Müller-Caspary[a,1,*], Florian F. Krause [a,1,**], Tim Grieb[a], Stefan Löffler[b,c,2], Marco Schowalter[a], Armand Béché[d], Vincent Galioit[e], Dennis Marquardt[a], Josef Zweck[e], Peter Schattschneider[b,c], Johan Verbeeck[d], Andreas Rosenauer[a]

[a]*Institut für Festkïrperphysik, Universität Bremen, Otto-Hahn-Allee 1, 28359 Bremen, Germany*
[b]*Institute of Solid State Physics, Vienna University of Technology, Wiedner Hauptstraße 8-10/E138, A-1040 Vienna, Austria*
[c]*University Service Centre for Transmission Electron Microscopy, Wiedner Hauptstraße 8-10/E052, A-1040 Vienna, Austria*
[d]*EMAT, University of Antwerp, Groenenborgerlaan 171, B-2020 Antwerpen, Belgium*
[e]*Institut für Experimentelle und Angewandte Physik, Universität Regensburg, Universitätsstraße 31, 93040 Regensburg, Germany*

Abstract

This study sheds light on the prerequisites, possibilities, limitations and interpretation of high-resolution differential phase contrast (DPC) imaging in scanning transmission electron microscopy (STEM). We draw particular attention to the well-established DPC technique based on segmented annular detectors and its relation to recent developments based on pixelated detectors. These employ the expectation value of the momentum transfer as a reliable measure of the angular deflection of the STEM beam induced by an electric field in the specimen. The influence of scattering and propagation of electrons within the specimen is initially discussed separately and then treated in terms of a two-state channeling theory.

A detailed simulation study of GaN is presented as a function of specimen thickness and bonding. It is found that bonding effects are rather detectable implicitly, e.g., by characteristics of the momentum flux in areas between the atoms than by directly mapping electric fields and charge densities. For strontium titanate, experimental charge densities are compared with simulations and discussed with respect to experimental artifacts such as scan noise. Finally, we consider practical issues such as figures of merit for spatial and momentum resolution, minimum electron dose, and the mapping of larger-scale, built-in electric fields by virtue of data averaged over a crystal unit cell. We find that the latter is possible for crystals with an inversion center. Concerning the optimal detector design, this study indicates that a sampling of 5 mrad per pixel is sufficient in typical applications, corresponding to approximately 10×10 available pixels.

Keywords: TEM, STEM, DPC, momentum transfer, field measurement, charge density measurement

1. Introduction

The control and measurement of solid state phenomena such as ferroelectricity, magnetism as well as spontaneous or piezoelectric polarisation in crystals is involved in or even paves the way for the engineering of many innovative nanoelectronic devices. Prominent examples are ferroelectric tunnel junctions [1, 2], spin light-emitting diodes [3–5] or InGaN-based light-emitting diodes [6–8]. Owing to its high spatial resolution and the strong coupling of electrons to electric and magnetic fields via the Lorentz force, transmission electron microscopy (TEM) is predestined for the

characterisation of such fields. The differential phase contrast (DPC) technique [9] has allowed for many impressive measurements in this domain.

As to the investigation of magnetic fields, magnetic domain walls in permalloy have been observed directly [10, 11], the vortex structure and domain wall widths of permalloy particles could be resolved [12] and magnetic vortex cores in permalloy could be shifted and pinned by magnetic fields [13].

Recently, DPC has been employed in studies of electrical properties, such as spontaneous polarisation in GaAs nanowires [14], piezoelectric fields in GaN/InGaN/GaN heterostructures [15], atomic-scale mapping of the electric field in $BaTiO_3$ [16] and dopant-modulated built-in electric fields in pn junctions [17].

As originally proposed for electron microscopy by Rose [9], DPC evaluates the asymmetry of intensity in the central part of diffraction patterns (the *Ronchigram*) by means of a split four-quadrant detector [10]. Most DPC measurements of both magnetic and electrical properties have relied on the established intuitive interpretation of the DPC

---

[*]Corresponding author. Tel.: +49 421 216 62267
[**]Corresponding author. Tel.: +49 421 216 62255
Email addresses: mueller@ifp.uni-bremen.de (Knut Müller-Caspary), f.krause@ifp.uni-bremen.de (Florian F. Krause)
[1]K. Müller-Caspary and F. Krause contributed equally to this work and thus share first authorship.
[2]Present address: Department of Materials Science and Engineering, McMaster University, 1280 Main Street West, L8S 4M1 Hamilton, ON, Canada.

signal being caused by a shift of the Ronchigram as a whole, reflecting the classically expected angular deflection of the electron beam in the specimen caused by the Lorentz force.

Some more recent works adopt a quantum mechanical interpretation of diffracted intensities in terms of probability currents [18, 19], ptychographic reconstructions of the object phase [20, 21] or the quantum mechanical expectation value for the electron momentum transfer [22]. The authors of this article recently related this expectation value to the projection of the electric field using Ehrenfest's theorem [23] in simulation and experiment, which allowed the measurement of atomic electric fields in $SrTiO_3$ [22].

While fields of a large extent of some tens of nanometers could successfully be characterized using segmented detectors and the conventional interpretation assuming a shift of the diffraction pattern as a whole, this approach has been shown to be inadequate for the quantification of atomic electric fields using contemporary aberration-corrected STEM at a resolution below 100 pm [22]. In this case the detailed intensity distribution in diffraction patterns has to be considered. On top of that, reliable field strengths are only obtained for very thin specimens. This situation hence demands a comprehensive study investigating the reliability of electric field characterization as a function of the spatial resolution in STEM, the specimen thickness as well as the scale at which electric fields vary, which is the goal of this article.

In the following, these issues are addressed via detailed simulation studies focused on electric fields in a GaN crystal. In section 2, we consider the measurement of the angular deflection from electron diffraction patterns in a quantum mechanical approach and point out limitations of DPC when employing segmented detectors. Section 3 treats the relation between angular deflection and electric field distribution in the framework of different models; the equivalence of one model with the phase object approximation is demonstrated. We then investigate the scattering of single atomic columns in section 4 which has the advantage that electron channeling can be studied apart from Bragg scattering, and interpret results in a simple s-state channeling model. Section 5 deals with the reliability of the electric field determination in GaN crystals as a function of specimen thickness and scattering amplitudes used in the simulation. The mapping of bonding charges is discussed via the comparison of data obtained in isolated atom approximation with density functional theory (DFT) data. Section 6 addresses the influence of inelastic scattering on the diffraction pattern. In section 7 we suggest a figure of merit for the spatial resolution and discuss requirements towards momentum space sampling and electron dose for given accuracy and precision as a guide for practical setups. Experimental and theoretical charge densities of $SrTiO_3$ are presented in section 8. We address the mapping of large-scale electric fields from atomic-resolution DPC data in section 9, followed by a discussion in section 10.

2. The angular deflection of electrons as a quantum mechanical observable

2.1. Diffraction patterns and the expectation value of the electron momentum transfer

In the Schrödinger picture of quantum mechanics, the wave function ψ is the central entity to describe the state of a quantum mechanical system. The wave function has different equivalent representations, for example $\psi(\mathbf{r})$ and $\psi(\mathbf{p})$ describe the same state in real and momentum space, respectively, with position $\mathbf{r}$ and momentum $\mathbf{p}$. Both representations are related by Fourier transform, i.e. $\psi(\mathbf{p}) \propto \mathcal{F}[\psi(\mathbf{r})]$. Considering image formation in a transmission electron microscope within the framework of Fourier optics, this fact is particularly interesting because the specimen exit plane and the back focal plane of the objective lens are also related by Fourier transform, giving rise to the Fraunhofer diffraction pattern in the back focal plane.

Thus, recording this pattern means recording the two-dimensional intensity distribution $I(\mathbf{p}_\perp) = |\psi(\mathbf{p}_\perp)|^2$ with $\mathbf{p}_\perp$ the vector of the lateral momentum parallel to the detector plane which is typically perpendicular to the optical axis. Furthermore, by the postulates of quantum theory,

$$\langle \mathbf{p}_\perp \rangle = \int d^2 p_\perp \, \mathbf{p}_\perp I(\mathbf{p}_\perp) \tag{1}$$

is the quantum mechanical expectation value of the lateral momentum, which, for a sufficient number of detected electrons, will be identical to the average lateral momentum. Without loss of generality, the initial average momentum can be chosen to be $\langle \mathbf{p}_\perp^0 \rangle = 0$ for the STEM probe incident on the specimen, so that Eq. (1) expresses the average momentum *transfer*. It is related to the scattering angle α by $h \cdot \sin \alpha = p_\perp \lambda$ with the relativistically corrected electron wavelength λ and the Planck constant h.

The previous considerations are well-established facts from quantum theory and Fourier optics. They do, however, reveal explicitly that the determination of the average momentum transfer does neither require the measurement of the phase of the wave function $\psi(\mathbf{p}_\perp)$, nor are any model assumptions to be made as to the interaction of the STEM probe with the specimen. At the same time the integration in Eq. (1) essentially condenses the two-dimensional intensity distribution $I(\mathbf{p}_\perp)$ with all its complexity into one single vector $\langle \mathbf{p}_\perp \rangle$ which nevertheless has a fundamental physical meaning.

2.2. Measurement of the average momentum transfer

It is this intuitive condensation of extensive, possibly complicated diffraction pattern data $I(\mathbf{p}_\perp)$ into one fundamental quantity $\langle \mathbf{p}_\perp \rangle$ that constitutes the appeal of average momentum transfer measurements [22]. However, the integral nature of Eq. (1) has important consequences for the design of the experimental setup because a suitable detector must realise the integration of the diffraction pattern coordinates $\mathbf{p}_\perp$ weighted by the local intensity
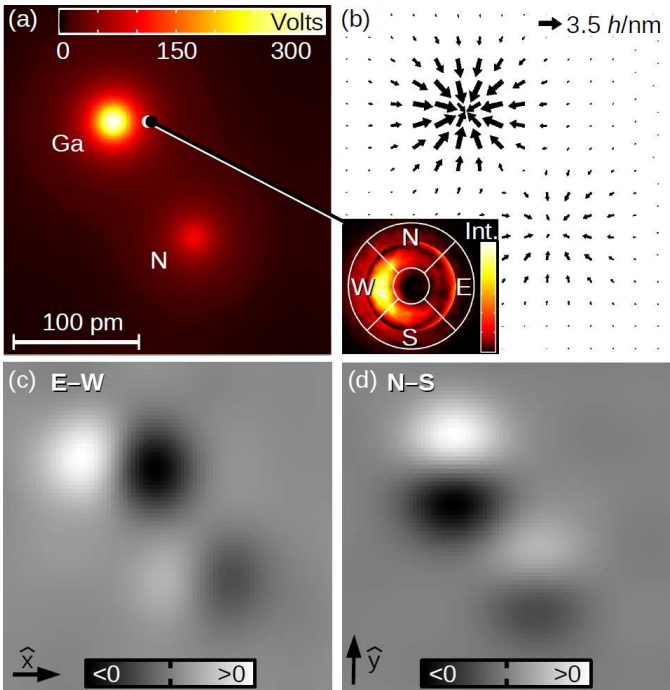
Figure 1: (a) Mean potential V_p of GaN calculated by DFT and projected along [11$\bar{2}$0]. (b) Momentum transfers for a STEM simulation (multislice) in the region depicted in (a). A specimen thickness of 2.2 nm and an aberration-corrected probe with 300 keV energy have been assumed. The momentum transfers were calculated from Eq. (1), h is Planck's constant. The inset shows a simulated Ronchigram for the indicated position in (a), and a conventional DPC detector with north, south, west, east segments. (c,d) Simulation of conventional DPC images using the detector shown in (b) for the region in (a). The contrasts in (c) and (d) qualitatively indicate a horizontal or vertical deflection, respectively.

Table 1: Probe parameters used for the multislice simulations.

acceleration voltage	300 kV
C_S of condenser	40 μm
semiconvergence angle	21 mrad (Scherzer)
probe defocus	−8.87 nm (Scherzer)

columns forming a "dumbbell". The mean projected potential of this area is shown in Fig. 1 (a).

The incident STEM probe was simulated corresponding to a contemporary aberration-corrected STEM instrument with a point resolution of 70 pm according to the parameters given in Tab. 1.

The vector field in Fig. 1 (b) depicts the resulting average momentum transfers according to Eq. (1) for a specimen thickness of 2.2 nm, exhibiting the atom positions as sinks of momentum transfer with a strength determined by the atomic number, being 4.4 times larger for Ga ($Z = 31$) than for N ($Z = 7$). The inset in Fig. 1 (b) exemplarily shows the central part of a diffraction pattern close to a Ga site as indicated. Obviously the dominant effect of the interaction with the crystal is a complex redistribution of intensity mainly within but particularly also outside the Ronchigram. While the calculation of the average momentum transfer in Eq. (1) takes this complexity fully into account, it becomes evident that a segmented ring detector, as indicated in white, integrates over a large azimuth of 90° and a wide range of scattering angles of typically 10 mrad or more [16]. Thus neither redistribution of intensity inside each segment nor intensity changes outside the segments can be detected. Besides that, conventional DPC signals will most likely depend heavily on the detector geometry, i.e. inner and outer ring radii and azimuthal orientation of the segments.

Nevertheless conventional DPC does indeed exhibit sensitivity to the angular deflection of the electrons in the present case as shown in Figs. 1 (c,d) which have been calculated by $W - E$ and $N - S$, respectively, corresponding to the signals of the west, east, north and south segments. Taking the asymmetries in both x- and y-direction together, the DPC images are intuitively satisfying because they can be interpreted such that the positively charged atomic nuclei attract the electrons of the STEM probe. This circumstance has probably motivated the interpretation of conventional DPC signals as being caused by a pure shift of the central beam, considered as a homogeneously illuminated disc apart from that. In that case, the momentum transfer can be calculated from signal differences between opposite segments via

$$\langle \mathbf{p}_\perp \rangle \propto [(W - E)\,\hat{x} + (N - S)\,\hat{y}]$$

with an appropriate proportionality factor as calibration. The following section will shed light on the validity of these assumptions.

$I(\mathbf{p}_\perp)$, or allow for it in postprocessing. Actually such a "center of gravity" or "first moment" detector had already been proposed in 1977 [24]. Recently, charge-coupled device (CCD) cameras for electron microscopy [25] reaching kHz frame rates [26, 27], delay-line detectors [28] or direct complementary metal-oxide-semiconductor (CMOS) cameras [29, 30] have been developed. Thereby the acquisition of four-dimensional data sets (a two-dimensional diffraction pattern for each STEM raster position) in acceptable time becomes feasible, enabling reliable measurements of $\langle \mathbf{p}_\perp \rangle$ at a dense STEM raster.

2.3. Limitations of conventional DPC

In contrast to the considerations of the previous section, DPC STEM has as yet primarily employed segmented ring detectors to investigate, e.g., electric fields, which we refer to as *conventional* DPC in the following. Its applicability for the quantitative measurement of $\langle \mathbf{p}_\perp \rangle$ will be considered next.

We used the STEMsim software package [31] to simulate diffraction patterns of a GaN crystal in [11$\bar{2}$0] orientation as a function of the position of the STEM probe in a region containing two closely neighbored Ga and N atom

3. Relating momentum transfer and electric field

3.1. Definitions

If a STEM raster of average momentum transfers is acquired, the maximum information that can be extracted from this two-dimensional field of two-dimensional vectors is another vector field of exactly the same dimensions. The ideal result would be the projected electric field

$$\mathbf{E}_\mathrm{p}(\mathbf{r}_\perp) = \frac{1}{\Delta z} \int_{\Delta z} \mathrm{d}z \, \mathbf{E}_\perp(\mathbf{r}_\perp, z), \qquad (2)$$

itself, where Δz is the thickness of the specimen along the optical axis. $\mathbf{E}_\mathrm{p}(\mathbf{r}_\perp)$ is related to the projected potential

$$V_\mathrm{p}(\mathbf{r}_\perp) = \frac{1}{\Delta z} \int_{\Delta z} \mathrm{d}z V(\mathbf{r}_\perp, z) \qquad (3)$$

by means of Maxwell's equations:

$$\mathbf{E}_\mathrm{p}(\mathbf{r}_\perp) = -\mathbf{grad}_\perp V_\mathrm{p}(\mathbf{r}_\perp). \qquad (4)$$

In the following it will be investigated to which extent a measurement of $\langle \mathbf{p}_\perp \rangle$ can be related to $\mathbf{E}_\mathrm{p}(\mathbf{r}_\perp)$.

3.2. Exploiting Ehrenfest's theorem

As long as expectation values are considered, the momentum $\langle \mathbf{p}_\perp \rangle$ in Eq. (1) can formally be related to the expectation value of the lateral electric field, $\langle \mathbf{E}_\perp \rangle$, in a straight forward manner: In classical physics, the time derivative of momentum equals force, which is equal to the Lorentz force in electrodynamics. In the absence of magnetic fields, only the Coulomb force $-e \cdot \mathbf{E}_\perp$ with elementary charge e remains. Importantly this still holds in quantum mechanics for expectation values according to the theorem of Ehrenfest [23, 32], yielding

$$\mathrm{d}\langle \mathbf{p}_\perp \rangle = -e \langle \mathbf{E}_\perp \rangle \mathrm{d}t \quad . \qquad (5)$$

Using the paraxial approximation where $\mathrm{d}t = \mathrm{d}z/v$ is the time an electron with speed v needs to propagate the distance $\mathrm{d}z$ along the optical axis, this reads

$$\mathrm{d}\langle \mathbf{p}_\perp \rangle = -\frac{e}{v} \langle \mathbf{E}_\perp \rangle \mathrm{d}z. \qquad (6)$$

Integrating over z within the specimen thickness Δz for a specific probe position $\mathbf{R}_\perp$ results in a formal expression for the expectation value of the momentum transfer

$$\langle \mathbf{p}_\perp \rangle(\mathbf{R}_\perp) = -\frac{e}{v}\Delta z \langle \mathbf{E}_\perp \rangle_\mathrm{p}(\mathbf{R}_\perp), \qquad (7)$$

where the definition of the projected expectation value of the electric field operator $\langle \mathbf{E}_\perp \rangle_\mathrm{p}(\mathbf{R}_\perp)$ is given by

$$\langle \mathbf{E}_\perp \rangle_\mathrm{p}(\mathbf{R}_\perp) = \frac{1}{\Delta z} \int_{\Delta z} \mathrm{d}z \iint \mathrm{d}^2 r_\perp \, \mathbf{E}_\perp(\mathbf{r}_\perp, z) I_{\mathbf{R}_\perp}(\mathbf{r}_\perp, z). \qquad (8)$$

See Fig. 2 for the definition of coordinates and a sketch of a typical Airy-shaped probe. Note that $I_{\mathbf{R}_\perp}(\mathbf{r}_\perp, z)$ is the
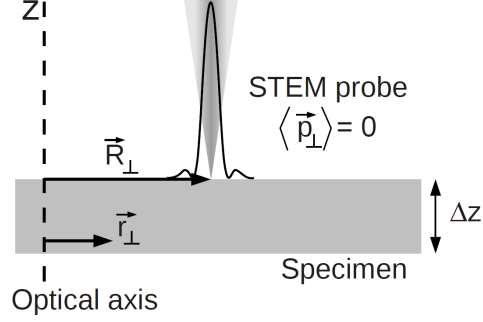

Figure 2: Illustration of the coordinate system used throughout this article. The STEM probe is incident along the z-direction, $\mathbf{R}_\perp$ is the position of the probe on the specimen of thickness Δz, $\mathbf{r}_\perp$ is a vector in the specimen plane assumed to be perpendicular to the optical axis. A typical Airy-shaped probe profile is also shown (not to scale), contrasted to the geometric model of conical incidence and a perfectly sharp probe.

three-dimensional intensity distribution within the specimen, resulting from a probe positioned at $\mathbf{R}_\perp$. No approximations or assumptions except for the well-justified paraxial approximation have been made so far.

Even though this argumentation started from a classical vantage point, one will get to the same result for fast electrons starting rigorously from the paraxial approximation of the Schrödinger equation

$$\frac{\partial}{\partial z}\psi(\mathbf{r}_\perp) = \mathrm{i}\left(\frac{\lambda}{4\pi}\Delta_\perp + \frac{2\pi e}{hv}V(\mathbf{r}_\perp, z)\right), \qquad (9)$$

The fully quantum mechanical derivation can be found in Ref. [22].

On the one hand, Eq. (7) directly relates the measured average momentum transfer $\langle \mathbf{p}_\perp \rangle(\mathbf{R}_\perp)$ to $\langle \mathbf{E}_\perp \rangle_\mathrm{p}(\mathbf{R}_\perp)$, which however is not independent of the probe intensity distribution, and therefore not a good measure from a material science standpoint. On the other hand, Eq. (8) can obviously not be solved easily for the quantity of interest, $\mathbf{E}_\mathrm{p}(\mathbf{r}_\perp)$, without approximations because $\mathbf{E}_\perp$ as well as $I_{\mathbf{R}_\perp}(\mathbf{r}_\perp, z)$ are in general functions of all three coordinates within the specimen. Furthermore, the probe intensity $I_{\mathbf{R}_\perp}(\mathbf{r}_\perp, z)$ inside the specimen is usually unknown and subject to propagation and scattering. Scattering itself is again dependent on the electric field making the solution a problem of self-consistency. With certain approximations for $I_{\mathbf{R}_\perp}(\mathbf{r}_\perp, z)$ however, as presented in the following, a direct relation between average momentum transfer $\langle \mathbf{p}_\perp \rangle(\mathbf{R}_\perp)$ and projected electric field $\mathbf{E}_\mathrm{p}(\mathbf{r}_\perp)$ can be derived.

3.3. Nonpropagating, point-shaped probe

If the electric field $\mathbf{E}_\perp$ in Eq. (8) was laterally homogeneous - at least inside the interaction volume, where $I_{\mathbf{R}_\perp}(\mathbf{r}_\perp, z) > 0$ - Eq. (7) would simplify to

$$\langle \mathbf{p}_\perp \rangle(\mathbf{R}_\perp) = -\frac{e \cdot \Delta z}{v} \cdot \mathbf{E}_\mathrm{p}(\mathbf{R}_\perp). \qquad (10)$$

4

The momentum transferred to a probe at position $\mathbf{R}_\perp$ would be directly proportional to the projected electric field and it would be independent of the shape of the probe. The simple relation in Eq. (10) would thus be ideal for the direct measurement of electric fields. From Eq. (9) it can furthermore be shown that in this specific case the momentum transfer would manifest solely in a shift of the otherwise unaltered Ronchigram which would allow for field quantification by conventional DPC.

On the one hand, assuming a constant electric field within the interaction volume appears as a too crude simplification. On the other hand, contemporary aberration-corrected STEM has reached minimum beam diameters of 50 pm [33] and better [34], so that one could argue that electric fields practically do not vary at such small scales and are quasi-constant at $\mathbf{R}_\perp$. It is noteworthy that Eq. (10) can also be derived directly from Eqs. (7,8) by assuming a point-shaped probe described by a Dirac delta function at the scan position $\mathbf{R}_\perp$,

$$I_{\mathbf{R}_\perp}(\mathbf{r}_\perp, z) = \delta(\mathbf{r}_\perp - \mathbf{R}_\perp), \qquad (11)$$

where we also neglect propagation inside the specimen. The beam therefore does not broaden inside the specimen and is z-independent. This model is equivalent to the assumption of a quasi-constant field, as $\mathbf{E}(\mathbf{r}_\perp)$ is constant in a singular point.

To study the applicability of the above model, we simulate the interaction of an aberration-corrected STEM probe for three different cases. First, the probe is propagated through a capacitor of infinite lateral extent, corresponding to a homogeneous electric field. Second, the simulation is repeated with a capacitor of a reduced lateral extent of 1.5 nm, corresponding to a piecewise homogeneous electric field, at least at a scale 20 times larger than the incident probe. Consequently, differences between both cases as to the shape of the Ronchigram and the consistency with Eq. (10) can be interpreted by means of a broadening of the probe beyond the extent of the capacitor due to propagation. Third, we neglect propagation and study solely the interaction of the probe with the potential of a GaN crystal projected into one slice, and check whether this single interaction alters the shape of the Ronchigram. For all simulations, probe parameters from Tab. 1 have been used.

First, STEM simulations were conducted for an electric field perpendicular to the optical axis, with a magnitude of 150 V/nm, an infinite lateral extent and various thicknesses. An exemplary diffraction pattern is shown in Fig. 3 and exhibits exactly the shift of a homogeneously illuminated Ronchigram expected for a homogeneous field. It is also visible that the measured momentum transfer $\langle \mathbf{p}_\perp \rangle$ is exactly following Eq. (10) for all specimen thicknesses.

Second, the dimensions of the field were reduced: Simulation results for a homogeneous field of the same strength but now spatially confined to a width of 1.5 nm are also displayed in Fig. 3. The probe was centered between the
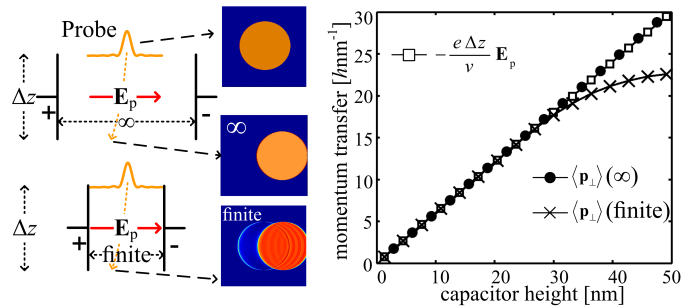

Figure 3: Behavior of the Ronchigram for a homogeneous field: The left part shows the simulated situation: A small probe is passing through a capacitor of height Δz and a lateral field $\mathbf{E}_\mathrm{p} = 150\,\mathrm{Vnm^{-1}}$. In the upper case the lateral extent of the capacitor is infinite, in the lower it is 1.5 nm, which is still small compared to the probe diameter of ≈ 100 pm. The central column shows the Ronchigram of the incident probe as well as that of the wave exiting both capacitors for $\Delta z = 50$ nm: In the finite case, a halo remains in place of the probe Ronchigram at a thickness of ≈ 25 nm. The graph on the right compares momentum transfer for both cases to the transfer expected from Eq. 10 with respect to Δz: For the finite extent a significant deviation is observed.

plates and more than 99.9 % of the incident intensity was localised inside the central half of the capacitor, so that the assumption of a constant field in the probe area is definitely satisfied in the incident plane. The average momentum transfer, however, is proportional to $\Delta z \mathbf{E}_\mathrm{p}$ only for capacitor heights below 25 nm. When the height increases further, it shows lower values than expected. This is caused by the propagation along the z-direction which increases the extent of the probe. At ≈ 25 nm parts of the probe leave the capacitor and the electric field is thus not constant in the entire interaction volume and the transfer of momentum decreases. This is not surprising, as the model assumptions are not fulfilled anymore.

Another interesting effect can be observed in the narrow capacitor: While most of the Ronchigram disc is shifted as in the infinite case, the sharp edge of the disc stays in position for $\Delta z > 25$ nm and does not move with increasing Δz, forming a halo. This is also an effect of the finite field area. Even if the probe is centered in the capacitor, its tails lap out into the field-free region after propagating 25 nm and more. Hence, the phase of this outer part of the probe is not altered and the corresponding intensity in the diffraction pattern is not shifted. These tails of the probe that are far from its center in real space belong to high spatial frequencies in reciprocal space, which causes the observed sharp halos. The same effect was described by Mahr et al. [35] for halos of diffracted discs near interfaces between materials with different lattice parameters.

It can be concluded from this study that electric fields which vary on scales much larger than the probe could be studied with the model of a point-shaped non-propagating probe, that leads to Eq. (10). However, with increasing specimen thickness the assumption of non-propagation can cause massive deviations from the model, even if the assumptions are valid in the incident plane. This is a first
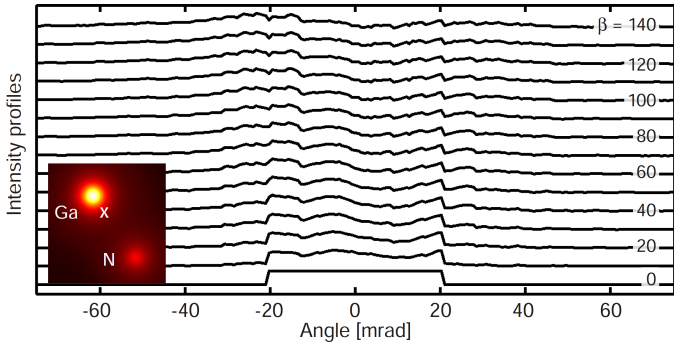
Figure 4: One-dimensional intensity profiles across the Ronchigram for a probe position on the connecting line between Ga and N as marked in the inset. The intensity is shown as a function of the strength of the projected potential, which has artificially been varied between $\beta = 0$ and 140 times its true value.

indication that a restriction to thin specimens will be necessary.

We third considered the interaction of the STEM probe with the potential of GaN projected along $[11\bar{2}0]$ for a beam position near a Ga site to test if the model of a point-shaped probe without propagation holds for realistic atomic fields. The incident wave function was multiplied with the phase grating $\exp(i\beta\sigma V_\mathrm{p}\Delta z)$ of one crystal slice with the projected potential V_p and interaction constant σ. In addition, V_p was scaled by a factor $\beta \in [0\dots140]$, representing the dependence on crystal thickness by means of multiples of the slice thickness of $0.32\,\mathrm{nm}$. In this way, the behavior of scattered intensities in the presence of electric field gradients in the illuminated area can be studied without propagation and influence of probe broadening.

The results are shown via the intensity profiles across the Ronchigram in Fig. 4. It can be seen immediately that already this kinematic approach reveals a complex intensity distribution inside the Ronchigram for any value of $\beta > 0$, which corresponds to specimen thicknesses of up to $50\,\mathrm{nm}$. The rectangular shape at $\beta = 0$ can be recognized partly up to $\beta = 60$, remaining centered in reciprocal space. This is clearly in contradiction to the predictions for a quasi-constant field. The first effect of the electric field is rather to deflect intensity towards the left edge inside the Ronchigram with increasing β than shifting the full Ronchigram. If β is raised further intensity is shifted beyond this edge.

To sum up, the deflection of the STEM probe by an electric field is usually not proportional to the field at the scan position. Moreover, Eq. (10) is violated if the electric field varies within the interaction volume, leading to a redistribution of intensity within the Ronchigram. This can happen either indirectly by propagation and consequent broadening of the STEM probe within the specimen or whenever the electric field varies already at the scale of the incident probe. The former can be avoided up to a certain extent with thinner specimens. The latter however must be taken into account even for contemporary, aberration-

corrected probes. In the following, we thus keep neglecting propagation but include the effect of electric field variations on extended probes.

3.4. Extended STEM probe without propagation

We now allow for an arbitrary intensity distribution $I_0(\mathbf{r}_\perp)$ of the STEM probe at the entrance surface of the specimen and assume that its shape is the same for all raster positions which then only cause a shift by $\mathbf{R}_\perp$. Since we neglect propagation the shape of the probe is independent of z, meaning $I(\mathbf{r}_\perp, z \geq 0) = I_0(\mathbf{r}_\perp)$. This model can therefore be expressed as

$$I_{\mathbf{R}_\perp}(\mathbf{r}_\perp, z) = I_0(\mathbf{r}_\perp - \mathbf{R}_\perp). \tag{12}$$

In experiments, $I_0(\mathbf{r}_\perp)$ can be measured indirectly by measuring the aberrations and defocus of the probe forming lenses. Note that directly acquiring a high magnification image of the probe on a camera is subject to aberrations of the imaging system of the microscope. Because this model is constant in z, inserting Eq. (12) in Eqs. (8) and (7) yields

$$\langle \mathbf{p}_\perp \rangle (\mathbf{R}_\perp) = -\frac{e \cdot \Delta z}{v} \cdot \mathbf{E}_\mathrm{PC}(\mathbf{R}_\perp), \tag{13}$$

using the definition

$$\begin{aligned}\mathbf{E}_\mathrm{PC}(\mathbf{R}_\perp) &= \int \mathrm{d}^2 r_\perp \, \mathbf{E}_\mathrm{p}(\mathbf{r}_\perp) I_0(\mathbf{r}_\perp - \mathbf{R}_\perp) \\ &= \mathbf{E}_\mathrm{p}(\mathbf{R}_\perp) \otimes I_0(-\mathbf{R}_\perp).\end{aligned} \tag{14}$$

The subscript "PC" stands for "probe convolved", as the integral is very similar to a convolution of the projected field with $I_0(\mathbf{R}_\perp)$. Nevertheless, it should be noted that as expressed by the second line Eq. (14) actually is a convolution with $I_0(-\mathbf{R}_\perp)$, which is the inversion of the probe intensity. This is of no elevated importance in the following considerations and is especially immaterial for rotationally symmetric probes, but should be kept in mind for experimental situations with asymmetric probe aberrations.

Equation (13) means that the expectation value for the momentum transfer is now directly proportional to the projection of the electric field, convolved with the probe intensity profile. Because this probe intensity is known, this allows a direct comparison to theoretical expectations from $\mathbf{E}_\perp$; as convolution is in principle invertible by a deconvolution, the effect of the probe extent can even, at least partially, be remedied.

As in the previous model, propagation is neglected but electric field gradients at the scale of the probe are incorporated now. Note that the convolution with the extended probe puts a resolution limit to electric field mapping here. As the preceding section showed, the neglect of propagation and the consequent independence of $I_{\mathbf{R}_\perp}(\mathbf{r}_\perp, z)$ from z will be problematic for thicker specimens, but as demonstrated in Ref. [22] it is a reasonable assumption for thin specimens. In this regard, this model is a compromise that

on the one hand spares one from the solution of the self-consistency problem in Eq. (8) but on the other hand is more accurate than the oversimplified model of a point-shaped probe as no assumptions about the probe shape, neither concerning extent nor symmetry, are made. Its scope and limits will be explored in the following sections.

3.5. Equivalence to the object phase gradient in phase object approximation

In the context of Eqs. (8) and (13) the question might arise, why the phase of the incident electron wave does not occur - only its intensity does. After all, the electric field affects the phase of the wave function. It could be claimed that these relations would apply only to rotationally symmetric probes or even only to perfectly aberration-corrected probes at perfect in-focus condition. Though this may seem astonishing, the derivations of the presented relations between average momentum transfer and projected fields are, except for the discussed assumptions, rigorous and no neglect of a potential phase curvature of the incident probe has been made.

In fact the model of an extended yet non-propagating probe is fully equivalent to the usage of the well-established phase object approximation (POA) as shall be derived in the following, where it is proven that the result of Eq. (13) is independently obtained in this established interaction model.

In case of the POA, the complete interaction with the specimen is expressed by a multiplication of the incident wave function with the phase object function

$$O(\mathbf{r}_\perp) = \exp\left(\mathrm{i}\varphi(\mathbf{r}_\perp)\right) \tag{15}$$

in real space, with the object phase $\varphi(\mathbf{r}_\perp)$. The intensity in the diffraction plane for an incident wave function ψ_0 that describes the probe positioned at $\mathbf{R}_\perp = (0,0)$ then reads

$$I(\mathbf{k}_\perp) = |\mathcal{F}\left\{O(\mathbf{r}_\perp)\psi_0(\mathbf{r}_\perp)\right\}|^2 = |O(\mathbf{k}_\perp) \otimes \psi_0(\mathbf{k}_\perp)|^2 \tag{16}$$

where the convolution theorem was used and $\mathbf{k}_\perp$ is the reciprocal coordinate associated with $\mathbf{r}_\perp$. Now, writing out the convolution and using the de Broglie relation $\mathbf{p} = h\mathbf{k}$, the fundamental Eq. (1) takes the following form:

$$\langle \mathbf{p}_\perp \rangle = h \int \mathrm{d}^2 k_\perp \, \mathbf{k}_\perp I(\mathbf{k}_\perp) = h \int \mathrm{d}^2 k_\perp \, \mathbf{k}_\perp$$
$$\times \int \mathrm{d}^2 \kappa_1 \, O(\mathbf{k}_\perp - \boldsymbol{\kappa}_1)\psi_0(\boldsymbol{\kappa}_1) \tag{17}$$
$$\times \int \mathrm{d}^2 \kappa_2 \, O^*(\mathbf{k}_\perp - \boldsymbol{\kappa}_2)\psi_0^*(\boldsymbol{\kappa}_2) \, .$$

By substituting $\mathbf{k}' = \mathbf{k}_\perp - \boldsymbol{\kappa}_1$ and $\boldsymbol{\kappa} = \boldsymbol{\kappa}_2 - \boldsymbol{\kappa}_1$ one further gets

$$\langle \mathbf{p}_\perp \rangle = h \int \mathrm{d}^2 \kappa \int \mathrm{d}^2 k' \int \mathrm{d}^2 \kappa_1$$
$$\times [\mathbf{k}' + \boldsymbol{\kappa}_1] \, O(\mathbf{k}')O^*(\mathbf{k}' - \boldsymbol{\kappa})\psi_0(\boldsymbol{\kappa}_1) \, \psi_0^*(\boldsymbol{\kappa} + \boldsymbol{\kappa}_1). \tag{18}$$

Using the identity $2\pi\mathrm{i}\mathbf{k}_\perp f(\mathbf{k}_\perp) = \mathcal{F}\left\{\mathbf{grad} f(\mathbf{r}_\perp)\right\}(\mathbf{k}_\perp)$ for Fourier transforms and once again invoking the convolution theorem this can be brought into the following form:

$$\langle \mathbf{p}_\perp \rangle = h \int \mathrm{d}^2 \kappa \int \mathrm{d}^2 \kappa_1 \, \boldsymbol{\kappa}_1$$
$$\mathcal{F}\left\{|O(\mathbf{r}_\perp)|^2\right\}(\boldsymbol{\kappa}) \, \psi_0(\boldsymbol{\kappa}_1) \, \psi_0^*(\boldsymbol{\kappa} + \boldsymbol{\kappa}_1)$$
$$+ \frac{h}{2\pi\mathrm{i}} \int \mathrm{d}^2 \kappa \, \mathcal{F}\left\{\mathbf{grad} O(\mathbf{r}_\perp) \cdot O^*(\mathbf{r}_\perp)\right\}(\boldsymbol{\kappa})$$
$$\mathcal{F}\left\{|\psi_0(\mathbf{r}_\perp)|^2\right\}(-\boldsymbol{\kappa}). \tag{19}$$

Note here, that $\mathcal{F}\{O^*(\mathbf{r}_\perp)\}(\mathbf{k}_\perp) = O^*(-\mathbf{k}_\perp)$.

Following Eq. (15) the absolute square of the object function is unity and also the relations

$$\mathbf{grad} O(\mathbf{r}_\perp) \cdot O^*(\mathbf{r}_\perp) =$$
$$\mathrm{i}\,\mathbf{grad}\varphi(\mathbf{r}_\perp) \exp\left(\mathrm{i}\varphi(\mathbf{r}_\perp)\right) \cdot \exp\left(-\mathrm{i}\varphi(\mathbf{r}_\perp)\right) = \mathrm{i}\,\mathbf{grad}\varphi(\mathbf{r}_\perp) \tag{20}$$

hold, hence

$$\langle \mathbf{p}_\perp \rangle = h \int \mathrm{d}^2 \kappa_1 \, \boldsymbol{\kappa}_1 |\psi_0(\boldsymbol{\kappa}_1)|^2$$
$$+ \frac{h}{2\pi} \int \mathrm{d}^2 \kappa \, \mathcal{F}\left\{\mathbf{grad}\varphi(\mathbf{r}_\perp)\right\}(\boldsymbol{\kappa}) \mathcal{F}\left\{|\psi_0(\mathbf{r}_\perp)|^2\right\}(-\boldsymbol{\kappa}). \tag{21}$$

The first term obviously represents the momentum of the incoming electron wave $\langle \mathbf{p}_\perp^0 \rangle$, while the second term represents the momentum transfer by the object. By inserting $\exp(2\pi\mathrm{i}\boldsymbol{\kappa} \cdot 0) = 1$ into the integral, this becomes an inverse Fourier transform at $\mathbf{R}_\perp = (0,0)$. Then, using the convolution theorem once more and exploiting that $|\psi_0(\mathbf{r}_\perp)|^2 = I_0(\mathbf{r}_\perp)$ the momentum of the object exit wave can be expressed as

$$\langle \mathbf{p}_\perp \rangle = \langle \mathbf{p}_\perp \rangle_0 + \frac{h}{2\pi} \left[I_0(\mathbf{R}_\perp) \otimes \mathbf{grad}\varphi(-\mathbf{R}_\perp)\right]_{\mathbf{R}_\perp=(0,0)} . \tag{22}$$

If the probe is shifted to $\mathbf{R}_\perp$, $I_0(\mathbf{r}_\perp)$ will obviously have to be replaced by $I_0(\mathbf{r}_\perp - \mathbf{R}_\perp)$. As discussed in Sec. 2.1 $\langle \mathbf{p}_\perp \rangle_0$ can be chosen to be zero by an appropriate coordinate system so that only momentum transfer is considered. Taking this into account, Eq. (22) can finally be written as

$$\langle \mathbf{p}_\perp \rangle(\mathbf{R}_\perp) = \frac{h}{2\pi} \int \mathrm{d}^2 r_\perp \, I_0(\mathbf{r}_\perp)\mathbf{grad}\varphi(\mathbf{r}_\perp - \mathbf{R}_\perp), \tag{23}$$

which is evidently equivalent to Eq. (13), as for a projected electrostatic potential $\varphi(\mathbf{r}_\perp) = \frac{2\pi e}{hv}\Delta z V_\mathrm{p}(\mathbf{r}_\perp)$ is fulfilled.

4. Single atomic columns as model systems

4.1. Single atomic columns within the s-state model

To study the average momentum transfer near atomic columns, a single column model system consisting of Ga-

atoms stacked in beam direction with the distance characteristic for a Ga-column in a GaN-crystal was investigated. The choice of this model allows for the investigation of the influence of atomic scale electric fields without effects owed to the crystal structure such as Bragg scattering. To gain a deeper understanding of the diffraction pattern dynamics indicated in the previous section, the formation of the electron distribution has been studied using the s-state channeling approach [36, 37] that has been successfully employed to explain the contrast mechanisms of annular bright field (ABF) imaging [38]. In this model, the electron wavefunction is expanded in eigenstates of the Hamiltonian $\hat{H}$ of Eq. (9) for electrons in the electrostatic potential of the atoms in paraxial approximation

$$\hat{H} = -v\left(\frac{h\lambda}{8\pi^2}\Delta_\perp + \frac{e}{v}V(\mathbf{r}_\perp, z)\right). \quad (24)$$

For this propagation, eigenstates of $\hat{H}$ fulfilling the relation

$$\phi_n(\mathbf{r}_\perp, z) = \phi_n(\mathbf{r}_\perp, z=0) \cdot \exp\left(-i\pi\frac{E_n}{E_0}\frac{z}{\lambda}\right) \quad (25)$$

can be found, meaning that the amplitudes of these states do not change while propagating through the crystal. Here, E_n is the eigen-energy of the state, which is negative for bound states, and E_0 is the kinetic energy of the incoming electrons. In analogy to atomic states, the lowest bound state that is rotationally symmetric is usually referred to as the 1s-state [36].

To study the intra-disc intensity, bound eigenstates for the Ga-columns were determined with the method of imaginary time [39]: By substituting z with $z' = -iz$ (in the paraxial approximation, z is equivalent to the propagation time), Eq. (9) becomes real and the propagation of the eigenstates is described by an exponential growth of the bound states and a decay of the unbound states. This also becomes clear if the substitution is done in Eq. (25).

If now a random initial wave function is propagated in z'-direction using a multislice scheme, the ground state component is predominantly amplified and hence after a sufficiently long calculation (usually a few hundred slices) solely the pure ground state remains. Further bound states can then be found successively by subtracting the projection of the wave function onto already found states between slices. This way all bound states can be determined.

A 1s-state ϕ_{1s} with eigen-energy of $E_{1s} = -116\,\text{eV}$ was found for $E_0 = 300\,\text{keV}$. All other bound states have eigen-energies larger than $-8\,\text{eV}$ and partially are not excited for reasons of parity, therefore in the following only the 1s-state is used for the evaluation. Following the approximation in Refs. [38, 40] the remaining bound states and all unbound states are assumed to propagate freely. Thus, the electron wave function ψ can be expressed as

$$\psi = \alpha_{1s}\phi_{1s} + (1 - \alpha_{1s})\phi_{\text{free}} \quad (26)$$

where α_{1s} is the quantum-mechanical overlap of the wave function and the 1s-state. ϕ_{free} is the normalised part of
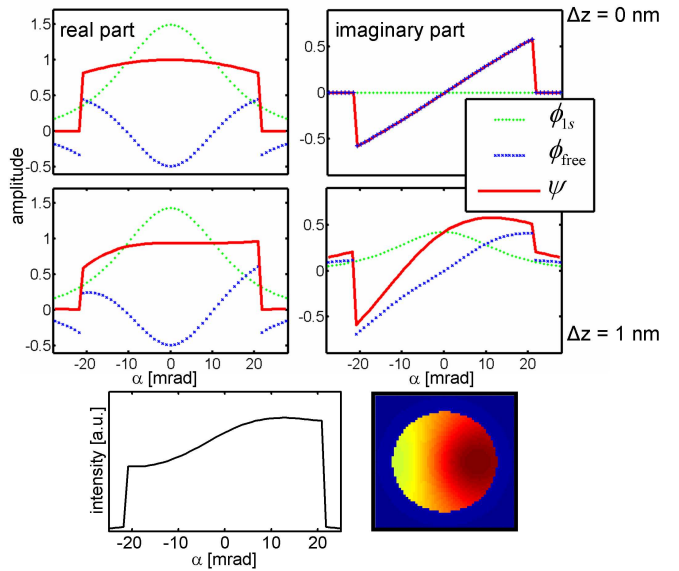

Figure 5: Propagation of a probe not centered on a column of Ga-atoms within the s-state model: The upper row shows central linescans through the p-space representation of the probe-wavefunction $\psi = \alpha_{1s}\phi_{1s} + (1 - \alpha_{1s})\phi_{\text{free}}$ as well as its components ϕ_{1s} and ϕ_{free} in the incident plane. The imaginary part is caused by a shift of $\Delta R_\perp = 0.15\,\text{nm}$ from the column center. In the middle row these wavefunctions are shown after propagation of 1 nm. Here the initial real and imaginary parts intermix, causing an asymmetry in the real part that leads to the asymmetric diffraction intensity displayed in the bottom row.

the wavefunction that is orthogonal to ϕ_{1s}. While ϕ_{1s} is solely determined by the specimen itself - in this case the Ga-column - both α_{1s} and ϕ_{free} depend on the actual wave function and have to be calculated for the incident wave function $\psi(z=0)$, which is identical with the STEM probe.

While the thickness dependence of ϕ_{1s} described by Eq. (25) is trivial, the free propagation of ϕ_{free} is best expressed in momentum space, where Eq. (26) takes the following form:

$$\psi(\mathbf{p}_\perp, z) = \alpha_{1s}\phi_{1s}(\mathbf{p}_\perp, z=0) \cdot \exp\left(-i\pi\frac{E_{1s}}{E_0}\frac{z}{\lambda}\right)$$
$$+ (1 - \alpha_{1s})\phi_{\text{free}}(\mathbf{p}_\perp, z=0) \cdot \exp\left(-\frac{i\pi}{h^2}p_\perp^2\lambda z\right) \quad (27)$$

Note that the phase factors have opposite signs, as E_{1s} is negative, therefore the phase shift during propagation is negative for ϕ_{1s} and positive for ϕ_{free}.

In absence of aberrations, the wave function $\psi(\mathbf{p}_\perp, z = 0)$ in the incident plane can be chosen to be a purely real top hat function for a probe perfectly centered on an atomic column, as has been assumed in investigations on ABF [40].

In this case the initial rotational symmetry of the diffraction pattern is conserved during the propagation, as Eq. (27) does not depend on the azimuth within the $p_\perp$-plane. If the probe however is shifted a small distance $\Delta\mathbf{R}_\perp$ from

8

the column center in real space, as it is during the scanning process, this is equivalent to the multiplication of $\psi(\mathbf{p}_\perp, z = 0)$ with a phase gradient $\exp\left(-\frac{2\pi i}{h}\Delta\mathbf{R}_\perp\mathbf{p}_\perp\right)$ in momentum space; therefore the probe wave function becomes complex at $z = 0$ as can be seen in the example shown in Fig. 5: The even real part of the wave function is modulated by a cosine while an odd imaginary part consisting of a sine emerges, which is completely part of ϕ_{free}, as the 1s-state is even and therefore has no overlap with odd functions. Though the diffraction pattern intensity still is rotationally symmetric at $z = 0$, the asymmetry of this odd imaginary part causes this to change during propagation.

With increasing z, the phases of both the ϕ_{1s} and the ϕ_{free} states are shifted according to Eq. (27), which effectively causes an intermixture of their real and imaginary parts: On one side, the imaginary part of $\phi_{\text{free}}(z = 0)$ is shifted into the real part; the sum of the resulting - now asymmetric - real part of ϕ_{free} and the real part of ϕ_{1s} therefore becomes asymmetric, too. On the other side, the symmetric real part of $\phi_{\text{free}}(z = 0)$ is shifted into the imaginary part, thereby causing a complementary effect. But here the different signs of the phase shifts applied during the propagation become important: As the 1s state is also shifted simultaneously but in the opposite direction, the complementary effect is weakened, especially at the disc edges, were $\Re\left(\phi_{1s}(z = 0)\right)$ and $\Re\left(\phi_{\text{free}}(z = 0)\right)$ are of the same magnitude. Hence, the asymmetry emerging in the real part is not compensated completely by the imaginary part and therefore an anisotropic diffraction intensity equivalent to a momentum transfer in the direction of the column center arises if the probe is not perfectly centered onto the column in this simple model.

As both ϕ_{1s} as well as ϕ_{free} are centered at $\mathbf{p}_\perp = 0$ and are propagated isotropically, this momentum transfer $\langle\mathbf{p}_\perp\rangle$, however, does not manifest in a shift of the entire diffraction disc but yields solely an intensity redistribution as can be observed in Fig. 5. For higher values of z, i.e. larger specimen thicknesses, very rich inner structures of the Ronchigrams occur.

4.2. Multislice simulations of single atomic columns

For a more accurate and profound investigation of the momentum transfer, the interaction of the STEM probe with the column of Ga atoms described above was then simulated with the multislice algorithm using STEMsim [31]. The radially symmetric column was scanned with the probe described in Tab. 1 on a numerical grid of 4096×4096 pixels spanning an area of 2×2 nm. As already expected from the s-state model outcomes, no significant shift of the disc was observed even for large specimen thicknesses.

The resulting momentum transfers $\langle\mathbf{p}_\perp\rangle$ evaluated from the simulated diffraction patterns are depicted in Fig. 6 for different column heights Δz. They are shown in direct comparison with $\langle\mathbf{E}_\perp\rangle_{\text{p}}$. In simulations the probe intensity is known everywhere in the specimen, making the direct evaluation of Eq. (8) possible here. As expressed in
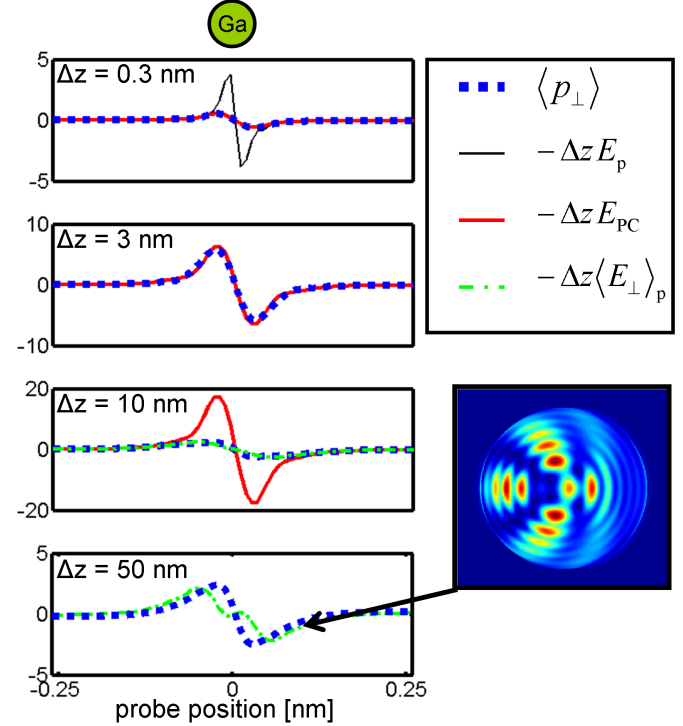

Figure 6: Average radial momentum transfer $\langle p_\perp\rangle$ simulated for a central linescan over a single Ga-column for different thicknesses Δz in comparison with the radial component of E_{p}, E_{PC} and $\langle E_\perp\rangle_{\text{p}}$. $\langle p_\perp\rangle$ and the electric fields are scaled in such a way that they are unit less and equal if Eqs. (7,10,13) are fulfilled. E_{p} is only plotted in the upper graph, as it gets very large compared to the other quantities for higher thicknesses; for the same reason E_{PC} is not shown for $\Delta z = 50$ nm. The image on the right bottom shows a typical Ronchigram for higher thicknesses and a probe position with a distance of 0.1 nm from the column center. While $\langle E_\perp\rangle_{\text{p}}$ agrees nicely with $\langle p_\perp\rangle$ for all thicknesses, E_{PC} deviates for thicknesses > 5 nm. As expected, E_{p} cannot be related to to $\langle p_\perp\rangle$ by simple proportionality.

9

Eq. (8), $\langle \mathbf{E}_\perp \rangle_p$ should always be directly proportional to $\langle \mathbf{p}_\perp \rangle$ and indeed this is found for almost all thicknesses, only for very thick specimens with $\Delta z > 40$ nm there are slight deviations, probably caused by numerical errors in the simulation.

Fig. 6 furthermore displays the values of $\mathbf{E}_p$ and $\mathbf{E}_{PC}$ which would be expected from the point-shaped and extended, non-propagating probe intensity models, respectively. It becomes apparent that, as already indicated by the previous investigations, $\mathbf{E}_p$ is not proportional to the average momentum transfer, not even for only $\Delta z = 0.3$ nm due to the extended beam shape. $\mathbf{E}_{PC}$ on the other hand actually shows a nice agreement with $\langle \mathbf{E}_\perp \rangle_p$ for thicknesses below ≈ 5 nm. For $\Delta z > 5$ nm the measured average momentum transfer starts to deviate from the values expected from $\mathbf{E}_{PC}$. For a 10 nm high column $\langle \mathbf{p}_\perp \rangle$ is less than half of its predicted value. At this Δz the propagation along z has broadened the beam so severely in comparison to the probe in the incident plane that the approximation of non-propagation becomes invalid. For small specimen thicknesses, however, this simplification appears to be sufficiently accurate allowing the direct field measurement from the average momentum transfer.

Once again it can be observed in the Ronchigram shown in Fig. 6, which was simulated for a probe position with more than one Ångström distance from the column, that a shift of the disc does not occur. The entire momentum transfer manifests itself almost entirely in intensity redistributions inside the disc.

It can be deduced from this study that, if Eq. (13) is to be used for field measurements, the specimen thickness has to be restricted to $\Delta z < 5$ nm.

5. Simulation study of field measurements in crystalline specimens

5.1. Reliability of field mapping using the model of an extended, non-propagating probe

In the practice of atomic-scale electric field mapping, Eq. (13) proves beneficial as it directly relates the average momentum transfer $\langle \mathbf{p}_\perp \rangle$ and the projected electric field convolved with the probe intensity, $\mathbf{E}_{PC}$, via a simple proportionality factor. For example, the momentum transfers in Fig. 1 b simulated for 2.2 nm thick GaN yield the electric field in Fig. 7, where it is superimposed on the mean projected potential V_P. While this result is plausible as atomic columns are sources of radial electric fields with a strength determined by the atomic number, Fig. 8 indicates that the simple relation between electric field and average momentum breaks down for larger crystal thicknesses. In the lower part the momentum transfers for a 10.2 nm thick specimen are depicted exemplarily which exhibit a strong anisotropy around atomic sites as to their magnitude and misleadingly suggest a larger atomic number for N than for Ga. Owing to dynamical scattering in the specimen it happens that Ronchigrams near the N site
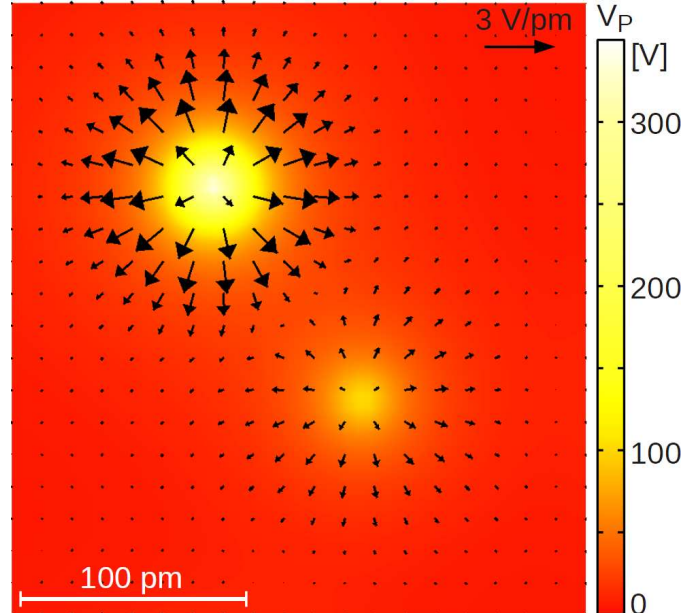

Figure 7: Electric field of GaN determined from the momentum transfers in Fig. 1 b using Eq. (13). The specimen thickness was 2.2 nm. For specimens this thin, the model of an extended nonpropagating probe allows a momentum-based field quantification which is accurate to 0.1 V/pm in the worst case.

suffer a comparable and partly stronger redistribution of intensity than those close to Ga, as seen for thicknesses of 6.1 and 10.2 nm in the top half of Fig. 8. However, by comparing the momentum transfers with the underlying mean projected potential V_P including some isolines, we see that the directions of the momentum transfers are mostly correct. In the following analysis, the reliabilities of direction and magnitude of the electric field determined from $\langle \mathbf{p}_\perp \rangle$ are hence treated separately.

To this end, we simulated thickness-dependent diffraction patterns as a function of the position of the STEM probe on a regular raster of 80×80 scan points in the GaN dumbbell region shown, e.g., in Fig. 1 a. A supercell of 15×15 unit cells in lateral direction on a numerical grid of 1500×1500 pixels was used here and for all following simulations of GaN. The diffraction space extended up to a spatial frequency of ≈ 90 nm^{-1}, enabling the study of the impact of a spatial frequency cutoff on the momentum transfer. This is necessary because the integral in Eq. (1) formally covers the whole momentum space whereas real detectors are limited in size. For each thickness and each spatial frequency cutoff, we calculated the momentum transfer field $\langle \mathbf{p}_\perp \rangle$ as in Fig. 1 (b) and Fig. 8, which we compared with the probe convolved projection average of the electric field, $\mathbf{E}_{PC}$.

Let us first consider the *direction* of $\langle \mathbf{p}_\perp \rangle$. For the model of an extended nonpropagating probe to hold, both quantities must be antiparallel according to Eq. (13). We thus define the angle

$$\varepsilon_1 = \sphericalangle\left(-\langle \mathbf{p}_\perp \rangle, \mathbf{E}_{PC}\right)$$
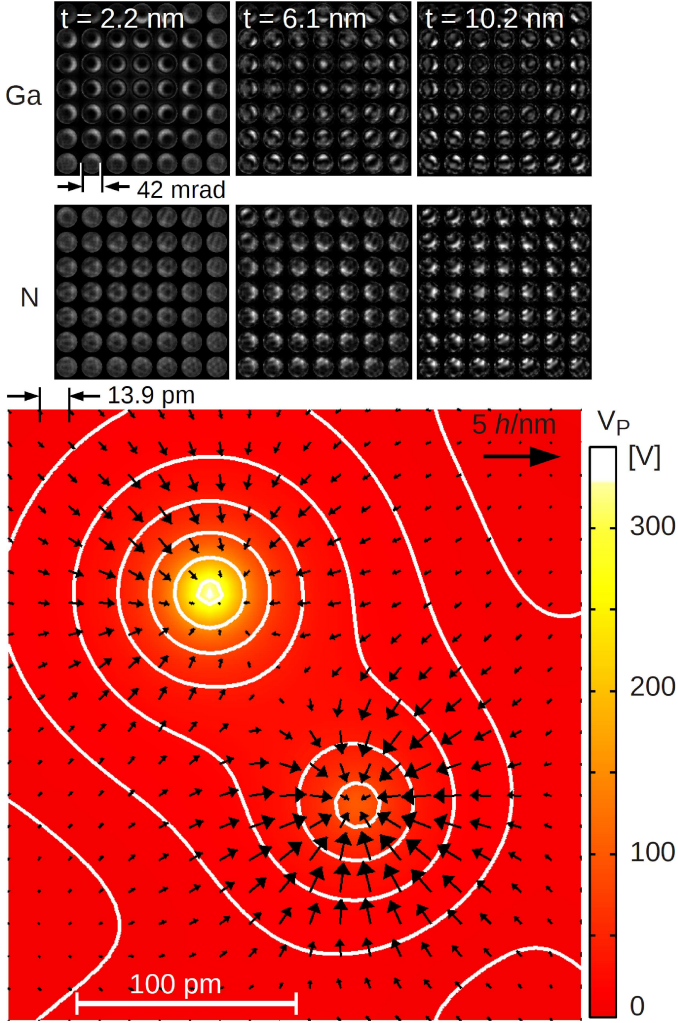
Figure 8: *Top:* Two-dimensionsional arrangement of Ronchigrams near Ga and N for three different specimen thicknesses showing a strong influence of nitrogen despite its low atomic number. *Bottom:* Vector field $\langle \mathbf{p}_\perp \rangle$ as in Fig. 1 b but for 10.2 nm specimen thickness, showing both an anisotropy near Ga and an enhanced sensitivity to N.

The Ronchigram scale bar indicates the diameter of the primary beam, i.e. 42 mrad. For better visibility, each fourth Ronchigram (momentum vector) of the simulation is shown, corresponding to a probe step size of 13.9 pm for adjacent Ronchigrams (momentum vectors) as indicated in the lower part.
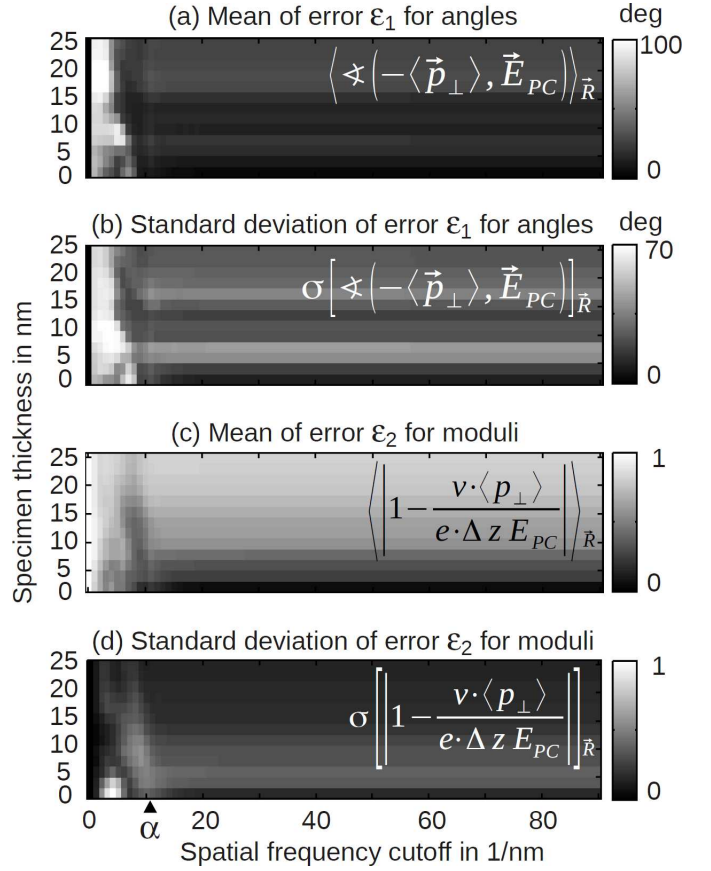
Figure 9: Comparison of directions and magnitudes of the electric field determined from momentum transfers $\langle \mathbf{p}_\perp \rangle$ and the electric field $\mathbf{E}_{PC}$ expected theoretically in dependence of spatial frequency cutoff used to calculate $\langle \mathbf{p}_\perp \rangle$, and specimen thickness. The orientational error is measured by ε_1, the error of field strength by ε_2, both expected to be 0 ideally. For brevity, only the mean and standard deviation of both errors calculated across the scan region are shown. The Ronchigram radius α is marked by the black triangle at the bottom.

to measure the error for the direction of the electric field one derives from $\langle \mathbf{p}_\perp \rangle$ at a certain scan position $\mathbf{R}_\perp$. Hence $\varepsilon = 0$ means that the direction of the electric field can be measured from $\langle \mathbf{p}_\perp \rangle$ without error, whereas $\varepsilon = 180°$ means that the electric field determined from the momentum transfer is antiparallel to the actual electric field in the specimen. To present results in a compact manner, we show only the mean $\langle \varepsilon_1 \rangle_{\mathbf{R}}$ and the standard deviation $\sigma[\varepsilon_1]$ of this error calculated from all raster positions in Figs. 9 (a,b).

From figure part (a) we see that the directions of the momentum transfers take values between 0 and 100°. Those cases where $\langle \mathbf{p}_\perp \rangle$ and $\mathbf{E}_{\mathrm{PC}}$ are more or less perpendicular are confined to spatial frequency cutoffs below $10 \, \mathrm{nm}^{-1}$ which corresponds to the radius of the Ronchigram as indicated by α at the bottom of the figure. For cutoffs beyond this value, ε_1 takes values below 5° for thicknesses below 5 nm, increasing up to 25° up to the maximum thickness of 25 nm. However, Fig. 9 (b) shows that ε_1 can vary significantly within the scan region at certain thicknesses, predominantly at 7.5 and 17.5 nm. The straight behavior for spatial frequencies beyond the Ronchigram radius shows that a detector slightly larger than the Ronchigram suffices in practice, at least for the thickness range considered here. We note that segmented detectors as in Fig. 1 (b) operate in this frequency range.

In a very similar manner we investigated the reliability of the *magnitude* of the electric field determined from $-v\langle p_\perp \rangle \cdot (e \cdot \Delta z)^{-1}$ according to Eq. (13). By definition of the relative error

$$\varepsilon_2 = \left| 1 - \frac{v\langle p_\perp \rangle}{e \cdot \Delta z \cdot E_{\mathrm{PC}}} \right|$$

and calculating mean $\langle \varepsilon_2 \rangle_{\mathbf{R}}$ and standard deviation $\sigma[\varepsilon_2]_{\mathbf{R}}$ across the scan region one obtains Figs. 9 (c,d), respectively. Again we find that a detector in diffraction space must at least cover spatial frequencies up to the Ronchigram radius α. Compared to the directional behavior, we observe that the average momentum $\langle \mathbf{p}_\perp \rangle$ is able to deliver the correct field magnitude only for specimen thicknesses below about 5 nm where Fig. 9 (c) depicts errors near 0. For larger specimen thicknesses the error increases rapidly up to $\varepsilon_2 \approx 0.8$ indicating that the momentum transfer can be only 20 % of the value expected by the model of Sec. 3.4. This effect can be attributed to propagation and (multiple) scattering inside the specimen.

To sum up the error analysis, electric field quantification by relating average momentum transfers $\langle \mathbf{p}_\perp \rangle$ and probe convolved electric fields $\mathbf{E}_{\mathrm{PC}}$ via a simple proportionality factor as described by Eq. (13) does only work for specimens with thicknesses $\lesssim 5 \, \mathrm{nm}$. This especially holds for the magnitude of the electric field. In all cases, the average momentum transfer must be determined using a spatial frequency cutoff not smaller than the Ronchigram radius. On the other hand, an expansion of the field of view for the diffraction pattern acquisitions beyond twice
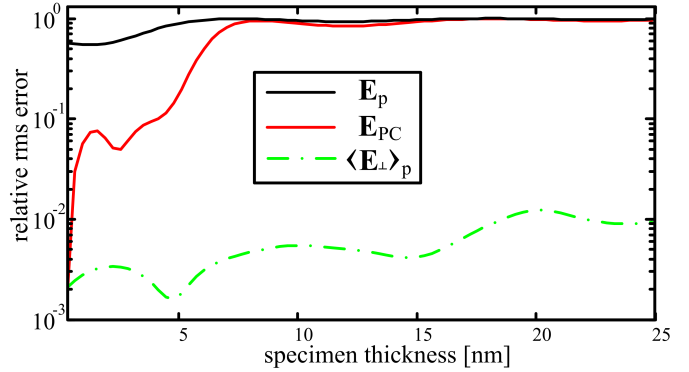

Figure 10: Relative root mean square (rms) deviation between the actual value of $\langle \mathbf{p}_\perp \rangle$ and its value calculated from $\mathbf{E}_{\mathrm{p}}$, $\mathbf{E}_{\mathrm{PC}}$ and $\langle \mathbf{E}_\perp \rangle_{\mathrm{p}}$ via Eqs. (7,10,13) for simulations of GaN with different thicknesses: As expected, relating $\langle \mathbf{p}_\perp \rangle$ to $\mathbf{E}_{\mathrm{p}}$ displayed as the thin black curve yields very large deviations between calculated and measured values even for very small thicknesses; the thick red curve representing the usage of a probe convolved field according to Eq. (13) stays below a relative rms error of 10% for specimens thinner than $\approx 5 \, \mathrm{nm}$. With momentum transfers calculated from $\langle \mathbf{E}_\perp \rangle_{\mathrm{p}}$ in dashed green a very good agreement is achieved for all thicknesses.

the Ronchigram radius does not improve the results significantly.

5.2. Thickness dependent accuracy of field measurement

To have a direct and simple measure for the appropriate thickness regime in which field measurements with the average momentum transfer can be done, the error corresponding to the different descriptions in Sec. 3, relating $\langle \mathbf{p}_\perp \rangle$ with either $\mathbf{E}_{\mathrm{p}}$, $\mathbf{E}_{\mathrm{PC}}$ or $\langle \mathbf{E}_\perp \rangle_{\mathrm{p}}$, was investigated solely in dependence of the specimen thickness. This was done for the same simulation parameters as used in the previous section for elastic scattering and without any intentional cutoff to the diffraction pattern.

The average momentum transfer $\langle \mathbf{p}_\perp \rangle$ expected from the models expressed in Eqs. (7,10,13) was computed and compared to the $\langle \mathbf{p}_\perp \rangle$ resulting from the simulations. To have one single measure for this error, direction and magnitude were not investigated separately but the root mean square (rms) of the difference between expected and simulated $\langle \mathbf{p}_\perp \rangle$, divided by the rms of the expected $\langle \mathbf{p}_\perp \rangle$ was used, where the averaging of the rms is performed over all scan positions inside a unit cell. The resulting relative rms error is more appropriate than the mean ratio as presented in Fig. 9 here to assess the accuracy for the different approximations in one error measure. In Fig. 9 the interstitial regions with small electric fields give an overproportional weight, which is not the case for the relative rms. Furthermore, it is automatically normalized to an intuitive scale typically ranging from 0 (no error) to ≈ 1 (deviation vector of same magnitude as expected momentum itself).

Fig. 10 shows the relative rms for the three probe models for various thicknesses. The improvement brought by relating $\langle \mathbf{p}_\perp \rangle$ to $\mathbf{E}_{\mathrm{PC}}$ instead of $\mathbf{E}_{\mathrm{p}}$ is very clear: The rms

error for $\mathbf{E}_{PC}$ is less than half as large as for $\mathbf{E}_p$ for specimen thicknesses below 4 nm. For such specimens measurement of $\mathbf{E}_{PC}$ should therefore be possible with good accuracy, which would allow the retrieval of the projected field itself by deconvolution, if the shape of the probe is known from the imaging conditions. For thicker samples substantial deviations occur as was also found for the single atomic column in Sec. 4.2. For $\langle \mathbf{E}_\perp \rangle_p$, the agreement is even better and does not change significantly with thickness. This is not surprising, as the derivation of Eq. (13) was generally exact. The found, small deviation can be attributed to numerical errors and slight inaccuracies due to the multislice approximation.

As discussed above, $\langle \mathbf{E}_\perp \rangle_p$ cannot be used to calculate the actual field without solving a self-consistency problem, usually the model of a non-propagating probe and hence $\mathbf{E}_{PC}$ will therefore be used. For this one will have to restrict oneself to very thin specimens of less than 4 nm thickness.

5.3. Bonding in gallium nitride

Up to here GaN has been studied with respect to DFT-based crystal potentials that account for a redistribution of charge density compared to isolated atoms. Owing to Maxwell's equations, this results in different electric fields so that different local momentum transfers can be expected. To investigate this effect the simulations above have been repeated using identical settings except that isolated atom potentials [41] have been used.

We start with the visual inspection of the intensity differences in the Ronchigrams at each scan position as mapped in Fig. 11 to see whether there is a certain region or angular range in which bonding affects the Ronchigrams preferentially. In the simulation for a 2.2 nm thick specimen shown in Fig. 11 we see that all scan positions exhibit a significant fingerprint of bonding in the Ronchigram intensities although the shape varies a lot among scan pixels. While intensity is redistributed from the Ronchigram center towards its edge in interstitial regions in the lower left and upper right part of the map, the opposite is true near the Ga site and between the atoms. For further analysis, we calculated the momentum transfer differences $\Delta \mathbf{p}_\perp = \langle \mathbf{p}_\perp \rangle^{DFT} - \langle \mathbf{p}_\perp \rangle^{ISO}$ as shown in Fig. 12. Superscripts refer to using DFT and isolated atom data in the simulations, respectively.

With a maximum of $0.2\, h/$nm the differences in Fig. 12 can take up to 5% of the actual momentum transfer $\langle \mathbf{p}_\perp \rangle^{DFT}$ in Fig. 1 b. Furthermore, the effects of bonding on $\Delta \mathbf{p}_\perp$ become obvious throughout the whole scan region. Together with the isolines for the potential difference $\Delta V_p = V_p^{DFT} - V_p^{ISO}$ depicted in grayscale in Fig. 12 we see that the vector field $\Delta \mathbf{p}_\perp$, which is perpendicular to the isolines, emerges from a source that is shifted 10 pm from the gallium site. The momentum transfers towards the nitrogen site and the interstitial area is larger for the DFT simulations than for the isolated atom simulations.
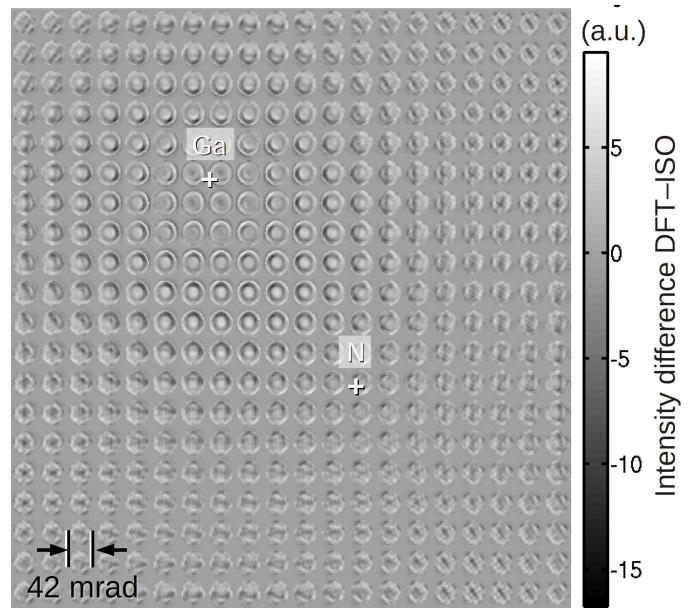

Figure 11: Two-dimensional arrangement of Ronchigram differences at 2.2 nm specimen thickness obtained by subtracting the isolated atom based [41] simulations from DFT-based simulations to illustrate the influence of chemical bonding on STEM diffraction patterns. The Ronchigram scale bar indicates the diameter of the primary beam, i.e. 42 mrad. For better visibility, each fourth Ronchigram of the simulation is shown, corresponding to a probe step size of 13.9 pm for adjacent Ronchigrams.
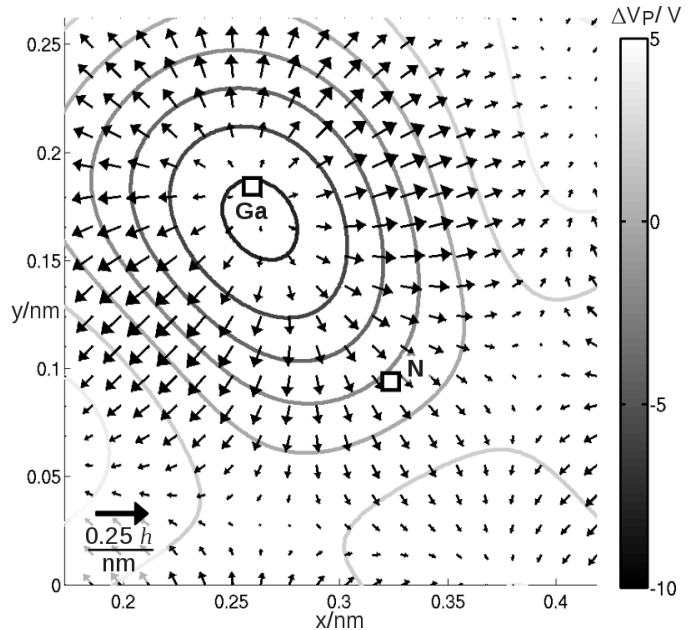

Figure 12: Difference vector field $\langle p_\perp \rangle^{DFT} - \langle p_\perp \rangle^{ISO}$ for 2.2 nm specimen thickness. The momentum transfer field $\langle p_\perp \rangle^{DFT}$ is shown in Fig. 1 b. The open squares indicate the positions of the Ga and N atom columns.
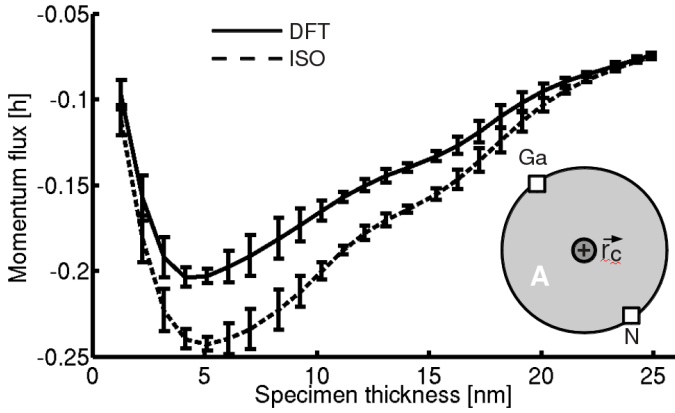
13

Figure 13: Simulations of the momentum flux as a function of specimen thickness in region A sketched in the inset for momentum transfers simulated with DFT and isolated atom [41] (ISO) potentials. The region A was chosen circular with a diameter equal to the bond length between Ga and N. The center of A has been varied by up to 7 pm from a position $\mathbf{r}_C$ halfways between the atoms to calculate the error bars.

Comparison with isolated atom results is only possible in simulations, so that there is no direct access to the data in Fig. 12 experimentally, of course. One solution would be to simulate the vector field $\langle\mathbf{p}_\perp\rangle^{ISO}$ exactly for the conditions at which $\langle\mathbf{p}_\perp\rangle^{DFT}$ has been measured which means that specimen thickness and orientation must be known very accurately. Alternatively one can also try to find a more robust quantity so as to demonstrate that bonding effects are directly visible in STEM. To this end, we assume that both atom positions can be detected with an accuracy of 7 pm in the following which is worse than contemporary benchmarks ranging from a few picometers [42] down to sub-picometer accuracy [43]. It turned out that, instead of examining the absolute field $\langle\mathbf{p}_\perp\rangle$ itself, the evaluation of its flux into certain areas A

$$\Phi_{p,A} = \oint_{\partial A} \langle\mathbf{p}_\perp\rangle\mathbf{n}\,\mathrm{d}s = \int_A \mathrm{div}\langle\mathbf{p}_\perp\rangle\,\mathrm{d}A, \qquad (28)$$

can exhibit clear fingerprints of charge redistributions due to bonding. Due to Gauss's law, $\Phi_{p,A}$ is related to the charge within A if Eqs. (10,13) are applicable. For example, we can choose a coordinate $\mathbf{r}_C$ halfways along the connecting line between Ga and N as origin and define a circle ∂A passing through both atom sites. Evaluating $\Phi_{p,A}$ in Eq. (28) as a function of specimen thickness yields the dependencies shown as solid and dashed curves in Fig. 13 for DFT and isolated atom data, respectively. The inset illustrates the region A from which the flux has been calculated in gray and the circle center $\mathbf{r}_C$ as a cross. According to the limited accuracy for the determination of the coordinates of atomic sites, $\mathbf{r}_C$ has been varied inside the dark gray region with 7 pm radius to give 35 different fluxes. The error bars drawn in Fig. 13 refer to the standard deviation of these fluxes. Both DFT and isolated atom data exhibit a very similar characteristic with a minimum near 5 nm specimen thickness and monotonic

increase beyond. However, bonding effects obviously lead to a $15-23\%$ larger flux in the thickness range of $4-15$ nm which is well separated from the isolated atom curve as to the error bars given. Measuring the momentum flux $\Phi_{p,A}$ in dependence of thickness or determining the thickness with 2 nm accuracy should therefore allow for the direct observation of bonding effects in STEM.

6. Influence of inelastic scattering

6.1. Thermal diffuse scattering (TDS)

The simulations to this point were conducted with a conventional multislice algorithm using Debye-Waller-damping and therefore broadened atomic potentials to account for thermal movement of the atoms and absorptive potentials for inelastic scattering. While this is accurate for the elastic interaction with the crystal, all inelastically scattered intensity is lost from the simulation and hence has not been considered for the momentum transfer investigations so far. Its influence on the momentum transfer is therefore investigated in the following.

Inelastic phonon interaction causing thermal diffuse scattering contributes to the diffraction pattern by a significant fraction - especially at higher specimen thicknesses - and the transferred momentum is quite large; hence high scattering angles are affected. Its impact on the measured momentum transfer has therefore to be investigated in order to draw conclusions as to the experimental measurability of the momentum transfer as discussed above.

To simulate TDS, frozen lattice (FL) simulations [44, 45] were performed with the same simulation parameters as described in the previous sections but with an increased size of the numerical grid of 1890×1890 pixels to ensure a sufficient sampling of the sharp atomic potentials. 120 different displacement configurations were averaged for the evaluated diffraction intensity. Results of these simulations are equivalent to a full quantum mechanical treatment of the inelastic phonon scattering [46].

The momentum transfer was determined from the diffraction pattern intensities and the two vector maps on the left hand side in Fig. 14 compare the momentum transfers evaluated from the FL simulation and from the previous conventional multislice calculations for thicknesses of 2.2 nm (upper row) and 25 nm (lower row). It becomes clear that TDS has a rather small influence on the measured $\langle p_\perp\rangle$, as both simulations deviate only little from each other; both directions and norms of the vectors are almost identical. Only in the vicinity to the Ga-column small differences can be observed for the thicker case. From the maps on the right hand side in Fig. 14 one can see that the difference is smaller than 3% in the vicinity of the atom columns at a thickness of 2.2 nm and the difference is smaller than 6% even in the regions in between the atoms where the average momentum transfer is small. The relative influence of TDS is therefore small and hence probably not measurable under experimental conditions. For 25 nm thickness,
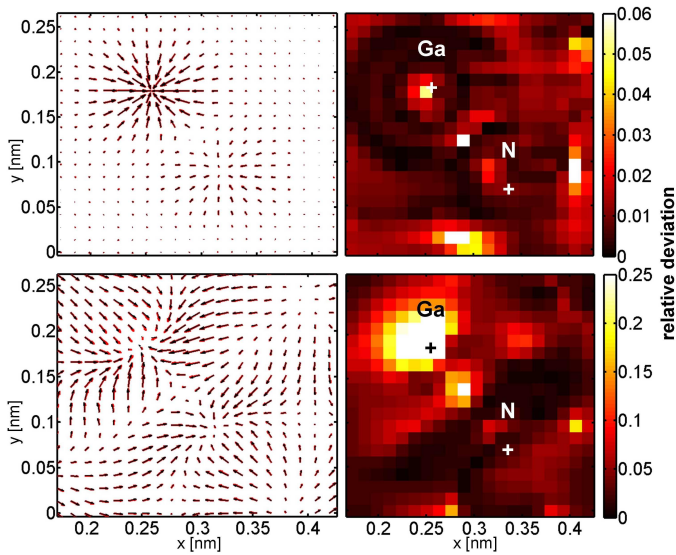
14

Figure 14: Comparison of momentum transfer for GaN in the area shown in Fig. 1: The upper row of images corresponds to a specimen thicknesses of 2.2 nm, the left image shows the momentum transfer from the conventional multislice simulations as black arrows and the FL results in red. On the right, the relative momentum difference is shown. The lower row shows analogous graphs for 25 nm specimen thickness.

the fraction of TDS-scattered intensity increases. Consequently, the relative effect takes values of up to 25% near the atomic columns.

It can be concluded that thermal diffuse scattering indeed has a significant influence on the measured momentum transfer for higher specimen thicknesses especially near heavy atomic columns. However, for small thicknesses as found necessary for field determination in the previous sections, the contribution of thermal diffuse scattering is smaller than the general deviations from the underlying model of Eq. (13).

6.2. Plasmon scattering

Plasmons - in particular the bulk plasmon - are the dominant features of electron energy loss (EEL) spectra. They are typically found for energy losses ≈ 25 eV. Therefore, the characteristic scattering angle associated with plasmon losses for a primary energy of $E_0 = 300$ keV is [47]

$$\theta_E = \frac{E}{E_0} \cdot \frac{E_0 + E_{\text{rest}}}{E_0 + 2E_{\text{rest}}} \approx 0.05 \, \text{mrad}, \qquad (29)$$

where E is the energy loss and $E_{\text{rest}} \approx 511$ keV is the electron's rest energy. This corresponds to a characteristic momentum transfer of $0.026 \, h\text{nm}^{-1}$ which is two orders of magnitude smaller than the typical momentum transfers in Bragg scattering caused by the electrostatic potential of the nuclei. According to the narrow scattering cone, plasmon-scattered electrons have almost the same angular distribution as elastically scattered electrons, which gives rise to the well-known preservation of elastic contrast in low-loss scattering [48].

Consequently, low-loss scattering can be included into the elastic channel for the purpose of the determination of atomic electric fields and charge densities.

6.3. Core-loss scattering

In terms of intensity, core-loss scattering is typically several orders of magnitude weaker [49] than low-loss scattering. As such, its influence on the (quasi-elastic) Ronchigrams is negligible. However, using energy filtering of the diffraction pattern, core-loss excitations can reveal additional information about the electronic states in the sample [50–52]. Thus, it is worthwhile to investigate the influence of core-loss scattering on Ronchigrams.

Fig. 15 shows the partial density of states (pDOS) for p-states of Nitrogen in GaN as calculated by WIEN2k [53]. The p_x and p_z orbitals are degenerate, while the p_y orbital has a different pDOS. Thus, choosing different energy slits effectively selects different conduction band states. From this data, Ronchigrams for inelastically scattered electrons were calculated using the mixed dynamic form factor (MDFF) formalism [51, 54, 55] to model the inelastic scattering and the multislice approach [56] for taking into account the elastic scattering both before and after the inelastic scattering event.

As is evident from Fig. 15, the asymmetry of the $p_{x,z}$ states and the p_y states is reflected most clearly by the Ronchigrams if the incident beam is positioned directly on a Nitrogen column. In such a situation, the Ronchigrams exhibit oval shapes with distinct major axes — a typical footprint of the different orientations of the orbitals. Therefore, valuable information about the characters of the conduction states as a function of energy can be derived from such energy-filtered Ronchigrams. In contrast to the purely elastic case, such an endeavor requires the determination of higher order moments of the scattering distribution, as the average momentum transfer (first order moment, Eq. (1)) is zero in this case.

If the beam is moved away from the N atoms, the Ronchigrams become asymmetric and start to exhibit a richer inner structure. Compared to the elastic case, they appear somewhat blurred due to the momentum distribution of core-loss transitions with a characteristic scattering angle of

$$\theta_E \approx 1 \, \text{mrad}. \qquad (30)$$

A detailed analysis of these phenomena is beyond the scope of this work.

7. Practical considerations

7.1. Investigation of attainable spatial resolution

Until here, all considerations were done for the same probe investigating gallium nitride. To achieve a comprehensive overview of the accuracy of field measurements from average momentum transfer a study of the attainable precision in dependence of the spatial frequency of the electric field was conducted:
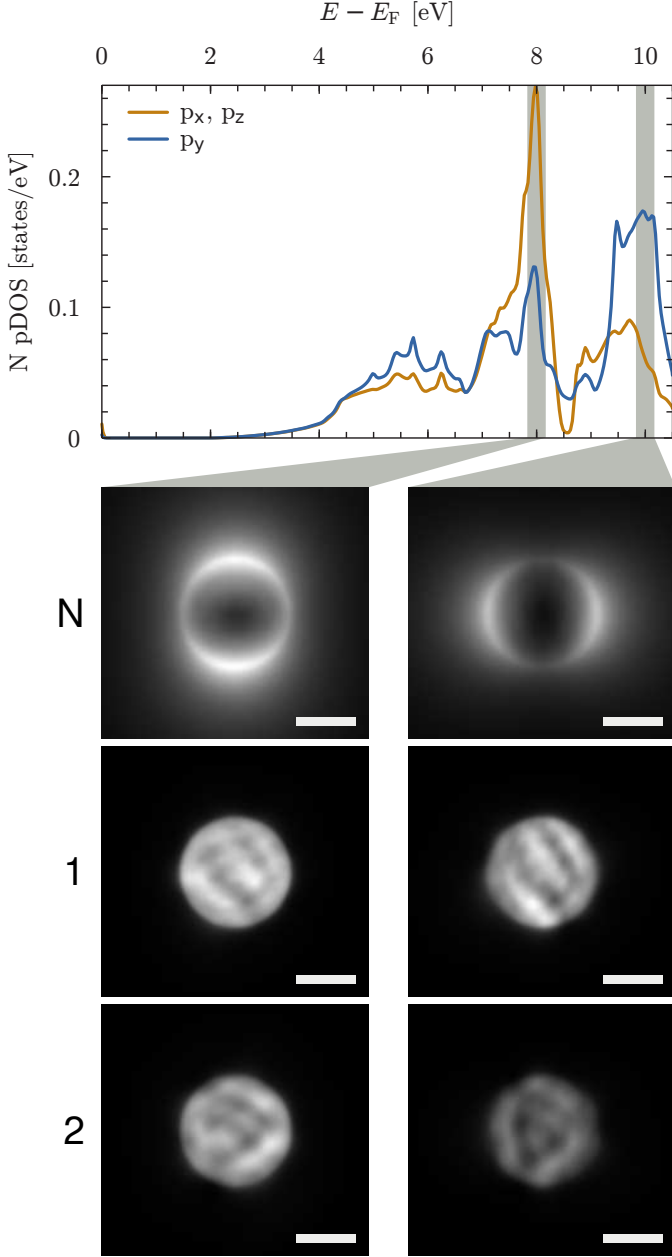
Figure 15: Comparison of the Ronchigrams after a Nitrogen core-loss excitation for two different excitation energies together with the Nitrogen pDOS for p-states. For the simulation, a 0.3 nm thick sample, a primary energy of 300 keV, and a convergence semi-angle of 21 mrad were used and the dipole-allowed transitions of the Nitrogen K-edge were calculated. The beam was positioned directly on a N column (top row), close to a Ga column (middle row) and far away from any atomic column at the edge of the unit cell (bottom row). Note that the labels p_x, p_y, and p_z refer to the symmetry-adapted coordinate system used by WIEN2k. All scale bars indicate 25 mrad and the intensities of the images in the middle and bottom rows were multiplied by 4 for better comparability with those in the top row.

To be able to make quantitative statements about achievable spatial resolution, a test-potential as depicted in Fig. 16a was used for the accuracy study. This potential oscillates with a constant amplitude of 200 V but descending period length in x-direction, while being constant in y-direction.

A linescan over this potential was simulated using the multislice method as described above with a very high sampling of 30 pixels per Angström and for thicknesses up to 25 nm. The resulting measured momentum transfer $\langle \mathbf{p}_\perp \rangle$ was compared to the transfer predicted from Eq. (13) assuming the probe-convolved field $\mathbf{E}_{PC}$ from Eq. (14). As discussed in Sec. 5.2 the relative rms error calculated by dividing the rms of the deviation between both values by the rms of the predicted value was used as a measure for the agreement.

The evaluation was done separately for each period of the potential, hence yielding thickness- and spatial feature-width resolved data. The results are shown in Fig. 16(b): As was already observed in previous sections, the agreement between $\langle \mathbf{p}_\perp \rangle$ determined from E_{PC} and the measured value is decreasing strongly for increasing specimen thickness. Furthermore, a reduction of the match is observed for narrower potential features. The dependency on both parameters is approximately linear. For potentials with characteristic lengths smaller than 1 Å the deviation stays below 20% for thicknesses up to 4 nm coinciding with the observations in Sec. 5.2.

To investigate the influence of the semiconvergence angle on the possible resolution, the simulations were additionally conducted with probes of 8 mrad and 42 mrad semiconvergence angle, respectively, and otherwise unaltered parameters. The results are shown in Fig. 16 (c) and (d).

It becomes obvious that the strongly increased size of the probe for the smaller convergence angle does not result in a severe reduction of accuracy for potential features larger than about half an Ångström. Nevertheless, for smaller structures the comparability of model and measurement drops drastically. This is caused by the fact that the probe extent itself is larger than these features, thus causing an almost complete levelling of the oscillating signal.

For the increased semiconvergence angle on the other hand, despite the very small probe, the rms is increased compared to the 21 mrad case for almost all thicknesses and spatial frequencies except for very thin specimens, where the results are actually better. This can be explained by the increased beam broadening appearing for this convergence. While the very small spot improves the resolution for the first layers, the broadening during the further propagation soon outweighs this advantage.

From this investigation, two conclusions can be drawn: First, the momentum transfer measurements for investigations of electric fields should be executed for specimen thicknesses below 4 nm to allow for evaluation on an atomic scale as confirming the findings of previous sections. For fields with larger extent, higher thicknesses will be accept-
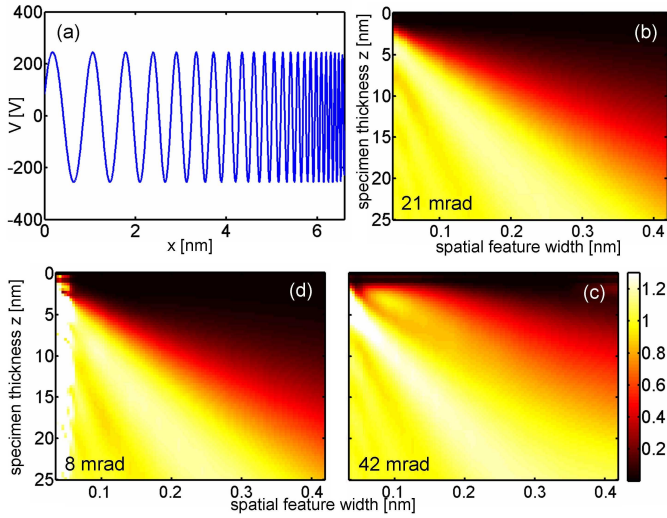
16

Figure 16: Figure of merit for the attainable spatial resolution of field determination by momentum measurements: (a) displays the used oscillating test-potential with amplitude of 200 V and varying spatial period. (b) shows the relative rms deviation of $\langle \mathbf{p}_\perp \rangle$ calculated from $\mathbf{E}_{PC}$ and the measured value of $\langle \mathbf{p}_\perp \rangle$ as a function of specimen thickness and spatial width of the potential features for a semiconvergence angle of 21 mrad. (c) and (d) show the same figure of merit for a semiconvergence of 8 mrad and 42 mrad, respectively. A relative rms deviation of ≈ 0 corresponds to very good agreement, while values ≈ 1 imply deviations of the same magnitude as the field itself.
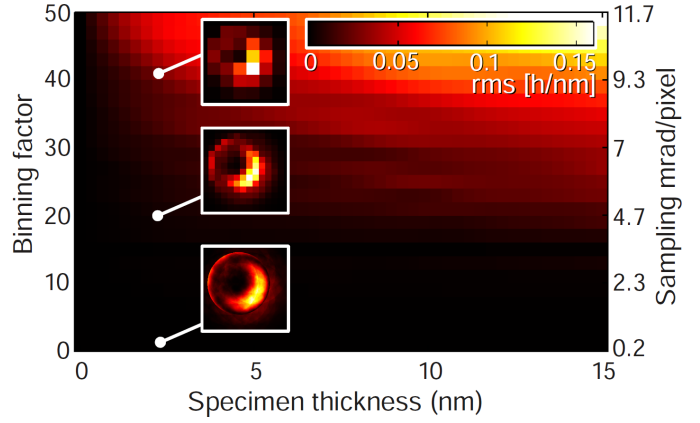

Figure 17: Reliability of the measurement of the average momentum transfer in GaN (simulation) as a function of the pixel size used for recording the diffraction pattern, and of the specimen thickness. The pixel size was varied by binning the diffaction patterns with odd factors. The colour-code expresses the rms deviation with respect to binning 1 (no binning). The insets exemplify Ronchigrams for binnings 1, 19 and 41 at a thickness of 2.2 nm.

able. Second, the semiconvergence angle does not necessarily need to be as large as possible for experiments of this kind. On the contrary: A very large convergence angle may even be counterproductive due to increased beam broadening.

7.2. Figure of merit for the momentum resolution

From the experimental point of view a figure of merit for the accuracy of momentum transfer measurements as a function of the sampling in diffraction space is desirable. This is because available ultrafast pixelated detectors [26, 27] achieve frame rates considerably beyond 1 kHz by binning, hence decreasing the resolution in recorded diffraction patterns. We can directly investigate this effect by using the thickness-dependent diffraction patterns simulated for GaN and calculate the average momentum transfer $\langle p_\perp \rangle$ as a function of binning. For all considerations until here, the full diffraction pattern resolution of 1500×1500 pixels spanning up to $\approx 90\,\mathrm{nm}^{-1}$ was used. In these simulations, the Ronchigram has a diameter of approximately 160 pixels. To investigate the sampling, we applied odd binnings between 1 (no binning) and 49 for all 80×80 diffraction patterns in a STEM scan at a certain thickness and calculated the vector field for the momentum transfer as a function of the binning factor. This study represents detectors down to a sampling of 3×3 pixels for the Ronchigram in the worst case. To present results in a compact manner, we calculated the deviation from the momenta obtained without binning in terms of the rms

deviation across the scan region. The result is depicted in Fig. 17 in dependence of specimen thickness and binning factor.

It is obvious that binnings larger than 19 yield inaccurate momentum transfers for all thicknesses larger than 5 nm whereas smaller thicknesses potentially allow for larger binnings. As to the detector design a binning of 19 means that the Ronchigram should be sampled by approximately 8×8 pixels. Considering that the detector must capture a region slightly larger than the Ronchigram, a pixel array with 10-15 pixels in one dimension is sufficient for the study of atomic electric fields here. Note that the present data corresponds to a semiconvergence angle of 21 mrad for the incident probe, so that a maximum effective pixel size of 5 mrad is recommended here. To get a visual impression of the effect of binnings 1,19 and 41 Fig. 17 contains example Ronchigrams at 2.2 nm thickness as insets.

7.3. Electron dose requirements

In a similar manner as for the momentum space sampling in the previous subsection, we also evaluated a figure of merit for the electron dose per Ronchigram. In a recent publication [57] a typical beam current of a non-probe-corrected FEI Titan microscope in high resolution STEM setting in the pA range was measured.

Using an ultrafast, pixelated detector [26, 27] a frame can be acquired within about 1 ms yielding a dose of about 6000 electrons for such a non-probe corrected machine. For a probe-corrected instrument equipped with a high-brightness gun the beam current can be about a factor of 100 higher.

We applied Poisson shot noise to selected Ronchigrams according to electron doses from $5 \cdot 10^3$ to $5 \cdot 10^6$ electrons per Ronchigram with an $1/\sqrt{N}$-equidistant spacing and calculated the deviation from the momentum obtained without noise in terms of the rms deviation as described in the
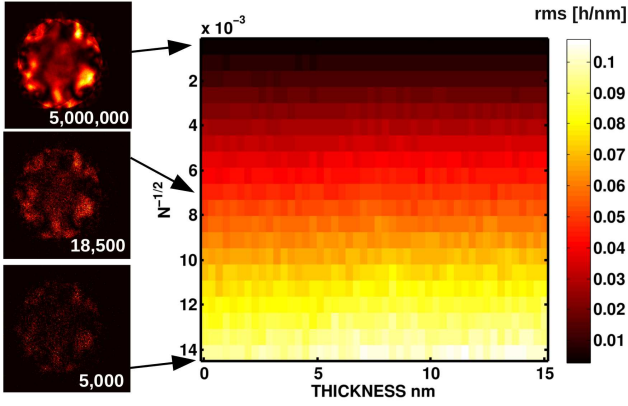
Figure 18: Root-mean-square deviation of the momentum transfer measured from Ronchigrams with noise to Ronchigrams without noise as a function of specimen thickness and electron dose. The shown exemplary Ronchigrams were calculated for doses of $5,000$, $18,500$ and $5 \cdot 10^6$

Figure 19: Charge density determination from average momentum transfers: (a) shows the probe convolved charge density ρ_{PC} according to Eq. (31) determined for SrTiO$_3$ in [100] projection from a 20×20 pixel average momentum transfer map after scan noise correction. The theoretically expected distribution is shown in (b). (c) and (d) show line scans from the red boxes in (a) and (b), respectively. The oxygen columns are clearly recognizable in the reconstructed charge density.

preceeding section. Instead of averaging over different scan positions we averaged over different realizations of the respective dose. The resulting rms deviation is plotted as a function of specimen thickness and $1/\sqrt{N}$ in Fig. 18. A linear decrease of the thickness independent rms deviation with $1/\sqrt{N}$ is found, which is in agreement with theoretical statistical considerations. An rms of about 0.05 h/nm is found already for 18500 electrons per Ronchigram, a condition that would be fullfilled for spot-size 9 on a non-probe corrected Titan and a millisecond frame time. In conclusion, dose is no limiting factor for the precision of average momentum measurement precision in modern instruments.

8. Charge density mapping in strontium titanate from experimental data

As discussed in detail in Ref. [22], the measurement of $\mathbf{E}_{PC}$ allows to calculate of the probe-convolved, projected charge density via the flux theorem of Gauß,

$$\rho_{PC}(\mathbf{R}) = I_0(-\mathbf{R}) \otimes \frac{1}{\Delta z} \int_{\Delta z} \mathrm{d}z \rho(\mathbf{R}) = \frac{1}{\varepsilon_0} \mathrm{div}\,\mathbf{E}_{PC}, \quad (31)$$

where ε_0 represents the vacuum permittivity.

As further demonstrated in Ref. [22], this relation does in fact allow the accurate determination of the projected charge density from simulated average momentum transfers. Prior knowledge of the nuclear charge distribution even gives access to the electron density.

When applying Eq. 31 to experimental data, one central obstacle is scan noise, which inevitably occurs in contemporary microscopes. This scan noise is caused partially by inaccurate positioning of the beam and especially due to specimen drift during the prolonged acquisition time that is necessary to get sufficient intensity for each Ronchigram. Due to this scan noise the actual scan positions do
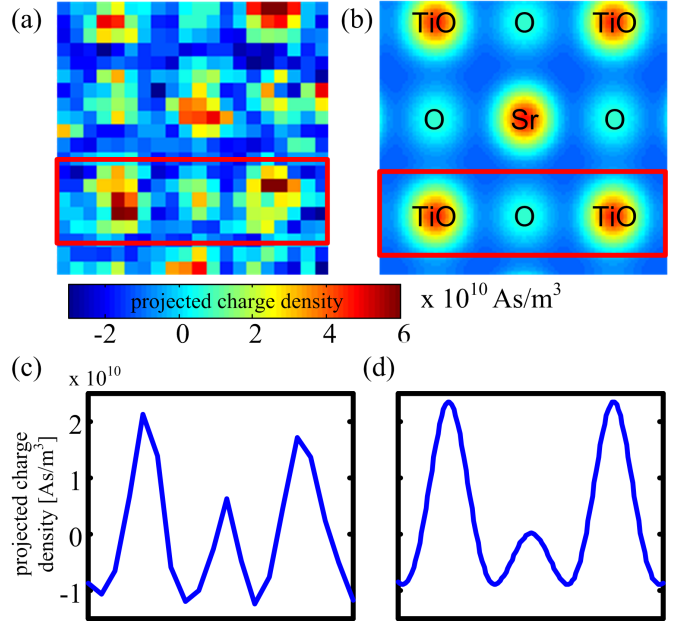
not lie on a regular grid; occasionally scan lines are even permuted due to specimen drift in the slow scan direction. This artifact will obviously have a massive impact on the result of the divergence operation.

Nevertheless, we attempted to determine the charge density from the experimental SrTiO$_3$ dataset presented in Ref. [22], which is a 20×20 pixel map of average momentum transfers acquired at a thickness of $\approx 2.5\,\mathrm{nm}$ in [100] projection. The Ronchigrams were recorded at a sampling of 128×128 pixels using an accelerating voltage of $300\,\mathrm{kV}$ and a probe semiconvergence angle of $21\,\mathrm{mrad}$ at a beam current of approximately $30\,\mathrm{pA}$.

To mend the scan noise artifacts as well as possible, an adaptation of the scan noise correction methods proposed in Ref. [58] to the relatively small number of only 20×20 pixels was made. For the correction the bright field signal extracted from the Ronchigrams was used. The summed intensity of the lines was used to determine the actual vertical position of each line by enforcing a vertically symmetric shape of each line of atomic columns which behaves monotonously from the center outwards. This worked well as the scan directions were aligned to the crystalline directions and allowed to assign all lines corrected vertical positions, which are not fully equidistant. For the horizontal alignment the shift between neighboring lines that resulted in the maximum normalized cross correlation was detected.

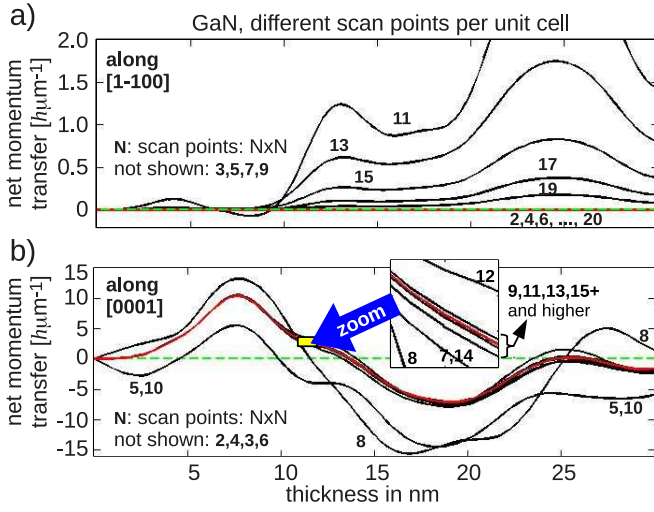The resulting, scan noise corrected coordinates for each

Figure 20: Simulation of the average momentum transfer in the Ronchigram averaged over one unit cell in GaN (*net momentum transfer*), (a) in the non-polar [1$\bar{1}$00] direction and (b) in polar [0001] direction. Each curve shows the thickness dependence for a different number of scanpoints per unit cell (N×N). In [1$\bar{1}$00] direction, curves for odd N converge to zero momentum transfer. Odd N<9 are not shown for reasons of clarity. In [0001] direction, the curves do not converge to zero momentum transfer (red line: N=20). Inset shows zoom for better separation of the single curves. N=2,3,4,6 is not shown for reasons of clarity.

pixel were then used to calculate the divergence in Eq. (31) and from that ρ_{PC}, which is displayed in Fig. 19a. An impact of scan noise is still visible, but a significantly better correction that is still based on objective, simple criteria is hard to achieve at this resolution.

In principle the directions and magnitudes of the average momentum transfers themselves could also be used for finding the true scan positions. We did however refrain from this to keep the information source for the scan noise correction independent from that of the charge density determination.

A comparison to the theoretically expected ρ_{PC} does, however, show a fair agreement. And as the linescans along one atomic row in Figs. 19c and d reveal, the scale of the charge density determined from the average momentum transfers is already quite accurate. Especially the reproduction of the light oxygen columns by this method is remarkable, as they are invisible in both the bright field and in the annular bright field images from the same dataset.

9. Mapping large-scale electric fields

Measuring the momentum transfer with the suggested method basically gives access not only to the atomic electric fields but also to influences on a larger scale such as crystal (mis-)orientation and long-ranging electric fields. In this section we investigate whether it is possible to quantify large-scale electric fields as they occur, e.g., within layered structures of polar materials [14] or in case of doping gradients [17].
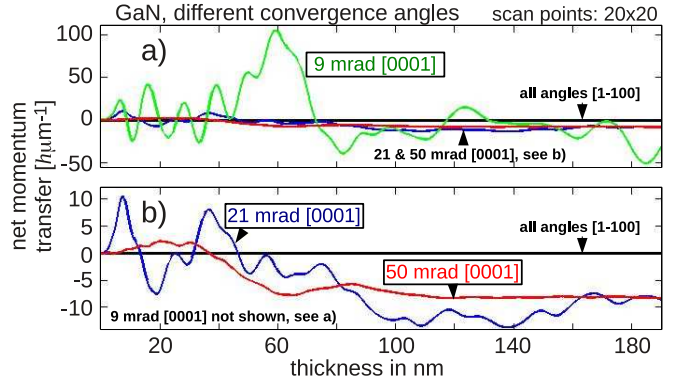

Figure 21: Simulation of the net momentum transfer in GaN as a function of thickness, using 20x20 scan points per unit cell. Each curve belongs to a different semi-convergence angle (9, 21 and 53 mrad). a) The net momentum transfer along the non-polar [1$\bar{1}$00] direction is zero for all convergence angles. In [0001] direction, variation and maximum absolut values are highest for 9 mrad convergence. b) For reasons of clarity, the curves for 21 and 53 mrad from a) are shown with smaller scaling on the vertical axis.

Quantification of atomic electric fields is limited by thickness due to the strong field gradients as it was previously shown and visualized in Fig. 9. In case of a homogeneous large-scale electric field, the momentum transfer should accumulate with specimen thickness (e.g. see Fig. 3). Nevertheless, typical electric fields, such as polarization fields in GaN-based alloys, are of the order of MV/cm, causing a momentum transfer which is four orders of magnitude smaller than those originating from atomic electric fields. In order to measure this small contribution to the momentum transfer, its net effect must be increased which can be done in two ways: On the one hand, the measurement can take place at a higher thickness, thereby strongly increasing the momentum transfer from the homogeneous field compared to the one from atomic fields. On the other hand, the momentum transfer could be averaged over a part of the crystal where the total momentum transfer originating from the atomic fields is completely compensated due to symmetry.

As wurtzite materials are typical candidates for large-scale electric fields from spontaneous and piezoelectric polarisation, (elastic) multislice simulations for pure GaN in [11$\bar{2}$0] zone axis were performed as above, but the whole Bravais cell was scanned instead of just a dumbbell region. The momentum transfers were determined from the Ronchigrams at each scan point and averaged over a complete unit cell (*net momentum transfer*) to check whether the momentum transfers caused by the atomic electric fields add to zero within a translatory invariant unit. Of course, the net momentum transfer critically depends on the number of scan points per unit cell. Fig. 20 displays the thickness dependence of the net averaged momentum transfer for different numbers of scan points (N×N, N= 2, ..., 20). The net transfer is separated (a) into the non-polar [1$\bar{1}$00] direction and (b) into the polar [0001] direc-

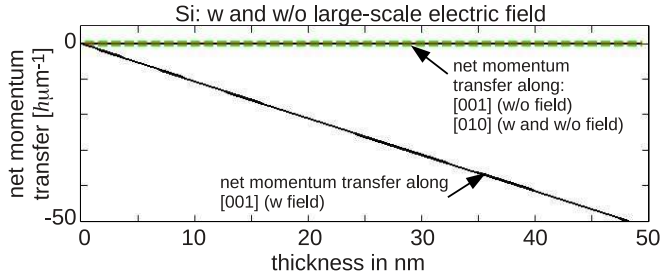Figure 22: Simulation of the net momentum transfer in Si as a function of thickness, including and not including an additional potential gradient (*w* and *w/o field*) of 10 MV/cm along [001] direction. The net momentum transfer vanishes for all cases except in the [001] direction in presence of an additional electric field: in this case, the absolute net momentum transfer increases linearly with thickness.

tion. Due to symmetry, the net transfer along [1$\bar{1}$00] vanishes for all even numbers of scan points. It converges towards zero with an increasing number of scan points in case of odd numbers. Contrarily, Fig. 20 (b) shows that the net momentum transfer does not vanish in [0001] direction but changes strongly with thickness. With an increasing number of scan points, it converges towards the red curve ($N = 20$). Typically, large-scale electric fields in GaN due to spontaneous or piezoelectric polarisation have a magnitude of a few MV/cm and occur along [0001] direction. From Fig. 20 (b) we conclude that a deflection of up to $7\,h\mathrm{nm}^{-1}$ corresponding to $15\,\mu\mathrm{rad}$ at a thickness of 18 nm is expected simply owing to the crystal structure, in particular the lack of inversion symmetry. Misinterpreted as caused by a large-scale, built-in polarisation field, one would obtain a field strength of 4 MV/cm. Note that piezoelectric fields are often found at interfaces in heterostructures where changes of the local chemical composition make the above situation even more complicated.

In Fig. 21 a) and b) the same net momentum transfer is shown up to a specimen thickness of 190 nm for different semi-convergence angles of 21 mrad (C_S-corrected), 9 mrad (non-corrected, only shown in a)) and for a hypothetical angle of 53 mrad. For 21 mrad the variations of the net momentum transfer along [0001] are slightly suppressed at thicknesses larger than 80 nm. Reducing the convergence angle is strongly worsening the variation with thickness. Instead, for a larger convergence angle, the thickness-dependent net deflection becomes smoother.

Fig. 22 shows the net momentum transfer for pure Si in [100] zone axis. The transfer separated in [001] and [010] direction completely vanishes (curves *w/o field*) due to the symmetry of the cubic crystal. The two curves named *w field* stem from a simulation with a super cell that containes a potential gradient of 10 MV/cm along [001] direction in addition to the atomic potentials of the crystal. Whereas the net momentum transfer is zero for the direction perpendicular to the field orientation, it increases linearly with thickness along [001] direction. Thus, in case of symmetric crystals, such as Si, a large-scale electric field

should be measurable by detecting the momentum transfer averaged over a unit cell without beeing negatively influenced by the atomic electric fields. Such a system is realised by strong doping gradients, e.g., along a p-n-junction.

10. Discussion and Summary

Considering original [9] and recent [16, 59] studies as well as the present one on DPC induced by electric fields, a discussion ought to focus on three main issues. Firstly, there is no doubt that atomic electric fields provide impressive contrast for both conventional segmented ring detectors [10, 60] and a pixel array as simulated here, making DPC especially attractive for the detection of light atoms. However, detecting atoms and understanding the experimental contrast quantitatively are different intentions.

Secondly, it is therefore necessary to understand differential phase contrast formation in detail in order to promote DPC to quantitative analysis. It is interesting to see that Rose [9] introduced STEM DPC from the attitude of the Ronchigram as an interference pattern formed by the primary beam and diffracted beams, in which separate detector segments ought to be placed in regions of constructive and destructive interference, respectively. Also Shibata et al. [16] explain intensity variations inside the Ronchigram by changes in the channeling of electrons. Aside from that, these intensity variations are not exclusively originating from the interference of diffracted discs, but also from thickness- and orientation-dependent scattering dynamics. For example, large-scale electric field mapping by conventional DPC employing nanometre-sized probes and well-separated diffraction discs has been discussed in terms of simulated channeling maps accompanying the measurements [17]. Consequently, the interpretation of DPC in terms of a shift of a homogeneously illuminated Ronchigram reveals some ambivalence in the STEM community. Moreover, it is assumed that the further improvement and characterisation [16] of segmented detectors is the key to the full quantification of electric fields. An explanation for the view on DPC as field-induced diffraction pattern shifts could be the success of this model in the investigation of magnetic domains [11, 12, 61, 62] in which magnetic fields practically do not vary at the scale of the STEM probe, which indeed leads to a shift of the diffraction pattern as a whole as demonstrated here for homogeneous electric fields. However, in cases where electric fields vary inside the illuminated specimen volume, this interpretation is oversimplified and will most likely yield inaccurate field strengths. It may be that this is the main reason why no quantitative field strength is given by Shibata et al. [16] in spite of excellent experimental high-resolution DPC data.

Thirdly, how can atomic-scale electric fields be measured quantitatively then? From the present work, we can give two possible answers to that question: Either indirectly by a combination of conventional segmented DPC

detectors [10, 60] with consistent dynamic simulations, or directly by measuring the average momentum transfer as presented here. As conclusions drawn in the former case rely on the congruence of simulation and experiment, there is a big challenge in reproducing the actual structure in the simulation model since it must contain all quantities to be measured, e.g., bonding or ferroelectric polarisation. Furthermore, the evaluation might exhibit some ambiguity because four [10] and even 16 [60] segment intensities extracted from piecewise integrations in reciprocal space can be caused by a variety of different diffraction patterns.

In case of the approach presented here the situation is different because the quantum mechanical momentum transfer from the specimen to the STEM probe is directly observed according to Eq. (1) with a precision given by the recording pixel array and the used electron dose. We note that the present approach provides an accurate measure of the average deflection of the STEM probe by the specimen, irrespective of the thickness range. Unfortunately, relating momentum transfer and projection average of the electric field in the specimen is conceptually hindered by two issues: The resolution is determined by the intensity distribution of the STEM probe, which basically enters by means of a convolution, and reliable electric field strengths are obtained for specimen with a thickness below 5 nm. On the one hand this is a challenging prerequisite as to specimen preparation, as has been pointed out for GaN and $SrTiO_3$ previously [22]. On the other hand, the present approach is predestined for the mapping of electric fields in the broad, upcoming sector of two-dimensional materials such as Graphene, MoS_2, WSe_2 or BN, for example.

The mapping of ionicity or electron redistribution due to chemical bonding as announced by Nellist [59] becomes now feasible. However, for GaN this study rather renders the detection of a fingerprint of bonding possible by measuring momentum fluxes in certain scan areas.

Furthermore the influence of inelastic scattering was investigated: The results of frozen lattice simulations suggest a rather small influence on the measured momentum transfers here - at least in the thickness regime in which meaningful field determinations are possible. For the regions with relevant electric field strengths, the relative deviations stay well below 5% at room temperature and could be reduced further by cooling the specimen to liquid nitrogen temperature, for which the mean square displacements of the atoms are reduced. A significant change of the elastic results due to phonon or core-loss scattering events can also be excluded. For core-losses an evaluation of higher order moments may allow the differentiation between different excitations of the same energy in terms of orbital orientation.

The attainable spatial resolution of field determination from average momentum transfer measurements was examined in simulations for different probe sizes. In agreement with the previous investigations, the study showed that an acceptable accuracy demands specimen thicknesses $\lesssim$ 4 nm and it appears that a probe semiconvergence of

≈ 20 mrad is optimal at 300 kV.

Concerning the recording hardware, one benefits from the finding that a detector size slightly larger than the Ronchigram is sufficient. Since fast detectors with a high detective quantum efficiency and low noise are required, experiments will benefit from scintillator-free direct electron detectors, whose performance as to the recording of diffracted discs in STEM with kHz rate has been demonstrated recently [26–28, 63–66]. Although such detectors constitute a leap in technology, typical STEM experiments are conducted at MHz rates. The fact that a sampling of approximately 5 mrad/pixel suffices deserves attention in this respect as an array of 10×10 pixels might be read out at such rates. It was further found that for contemporary instruments and cameras, the electron dose per acquired Ronchigram should not state any significant limitation to the precision of average momentum transfer measurements.

Taking all these prerequisites into account, it was possible to map the projected charge density in strontium titanate from the electric field measured experimentally via average momentum transfers and electric fields presented previously [22]. After correcting for scan noise, the charge density is in good agreement with theoretical expectations, whereas the sensitivity to the ionicity of atomic columns is left as a future task.

Particular care should be taken when measuring built-in electric fields at the resolution of a unit cell or larger. Due to the fact that typical field strenghts are $0.1-1$ V/nm, thus $3-4$ orders of magnitude smaller than atomic electric fields, built-in fields are preferably measured at higher specimen thicknesses in the range of a few 100 nm to be sensitive to small momentum transfers. However, an important prerequisite is that the diffraction pattern complies with Friedel's law [67], at least in the direction where the built-in field is studied. In that case, the net deflection of the HRSTEM probe as caused by the built-in field can be calculated by summing all momentum transfers within a translational invariant unit. Note that also low-resolution STEM, corresponding to non-overlapping diffraction discs, can exhibit asymmetric Friedel pairs. A remedy for investigating, e.g., polarity in wurtzite GaN or AlN structures, wurtzite GaP or GaAs nanowires would be the recording of the undiffracted beam in low-resolution STEM mode, and subsequent determination of its geometric position by algorithms developed for strain analysis by nano-beam electron diffraction [35, 68].

11. Conclusion

A comprehensive study on the characterisation of electric fields based on average momentum transfer measurements was presented. The relation of field and momentum transfer was theoretically discussed and analysed in simulations of various model systems as well as realistic crystalline specimens. For thin samples, accurate measurement of atomic electric fields was found to be quan-

titatively possible. The influence of inelastic scattering processes was simulated and can be neglected for such measurements. The attainable accuracy in dependence of both spatial resolution and momentum space sampling was investigated and the relation between electron dose and the achievable precision was studied. Furthermore we demonstrated mapping of the projected charge density in strontium titanate in good agreement with theoretical expectations. By averaging the momentum transfer over larger scan regions, the method can also be applied to measurement of large-scale electric fields if certain crystal symmetries are given.

Acknowledgements

References

References

[1] Z. Wen, C. Li, D. Wu, A. Li, N. Ming, Ferroelectric-field-effect-enhanced electroresistance in metal/ferroelectric/semiconductor tunnel junctions, Nature Materials 12 (2013) 617–621.

[2] E. Y. Tsymbal, H. Kohlstedt, Tunneling Across a Ferroelectric, Science 313 (2006) 181–183.

[3] W. Löffler, D. Tröndle, J. Fallert, H. Kalt, D. Litvinov, D. Gerthsen, J. Lupaca-Schomber, T. Passow, B. Daniel, J. Kvietkova, M. Grün, C. Klingshirn, M. Hetterich, Electrical spin injection from ZnMnSe into InGaAs quantum wells and quantum dots, Appl. Phys. Lett. 88 (2006) 062105.

[4] J. Beyer, I. A. Buyanova, S. Suraprapapich, C. W. Tu, W. M. Chen, Spin injection in lateral InAs quantum dot structures by optical orientation spectroscopy, Nanotechnology 20 (2009) 375401.

[5] G. Kioseoglou, M. Yasar, C. H. Li, M. Korkusinski, M. Diaz-Avila, A. T. Hanbicki, P. Hawrylak, A. Petrou, B. T. Jonker, Intershell Exchange and Sequential Electrically Injected Spin Populations of InAs Quantum-Dot Shell States, Phys. Rev. Lett. 101 (2008) 227203.

[6] S. Nakamura, T. Mukai, M. Senoh, Candela-class high-brightness InGaN/AlGaN double-heterostructure blue-light-emitting diodes, Applied Physics Letters 64 (1994) 1687–1689.

[7] K. Iso, H. Yamada, H. Hirasawa, N. Fellows, M. Saito, K. Fujito, S. P. DenBaars, J. S. Speck, S. Nakamura, High Brightness Blue InGaN/GaN Light Emitting Diode on Nonpolar m-plane Bulk GaN Substrate, Jpn. J. Appl. Phys. 46 (2007) 960–962.

[8] H. Masui, H. Asamizu, T. Melo, H. Yamada, K. Iso, S. C. Cruz, S. Nakamura, S. P. DenBaars, Effects of piezoelectric fields on optoelectronic properties of InGaN/GaN quantum-well light-emitting diodes prepared on nonpolar (1$\bar{1}$0) and semipolar (1$\bar{2}$2) orientations, Journal of Physics D: Applied Physics 42 (2009) 135106.

[9] H. Rose, Nonstandard imaging methods in electron microscopy, Ultramicroscopy 2 (1977) 251–267.

[10] J. Chapman, P. Batson, E. Waddell, R. Ferrier, The direct determination of magnetic domain wall profiles by differential phase contrast electron microscopy, Ultramicroscopy 3 (1978) 203–214.

[11] C. W. Sandweg, N. Wiese, D. McGrouther, S. J. Hermsdoerfer, H. Schultheiss, B. Leven, S. McVitie, B. Hillebrands, J. N. Chapman, Direct observation of domain wall structures in curved permalloy wires containing an antinotch, Journal of Applied Physics 103 (2008) 093906.

[12] R. Ploessl, J. N. Chapman, A. M. Thompson, J. Zweck, H. Hoffmann, Investigation of the micromagnetic structure of cross-tie walls in permalloy, J. Appl. Phys. 73 (1993) 2447–2452.

[13] T. Uhlig, M. Rahm, C. Dietrich, R. Höllinger, M. Heumann, D. Weiss, J. Zweck, Shifting and Pinning of a Magnetic Vortex Core in a Permalloy Dot by a Magnetic Field, Phys. Rev. Lett. 95 (2005) 237205.

[14] B. Bauer, J. Hubmann, M. Lohr, E. Reiger, D. Bougeard, J. Zweck, Direct detection of spontaneous polarization in wurtzite GaAs nanowires, Applied Physics Letters 104 (2014) 211902.

[15] M. Lohr, R. Schregle, M. Jetter, C. Wächter, T. Wunderer, F. Scholz, J. Zweck, Differential phase contrast 2.0 - Opening new "fields" for an established technique, Ultramicroscopy 117 (2012) 7–14.

[16] N. Shibata, S. D. Findlay, Y. Kohno, H. Sawada, Y. Kondo, Y. Ikuhara, Differential phase-contrast microscopy at atomic resolution, Nature Physics 8 (2012) 611–615.

[17] N. Shibata, S. D. Findlay, H. Sasaki, T. Matsumoto, H. Sawada, Y. Kohno, S. Otomo, R. Minato, Y. Ikuhara, Imaging of built-in electric field at a p-n junction by scanning transmission electron microscopy, Scientific Reports 5 (2015) 10040.

[18] A. Lubk, J. Zweck, Differential phase contrast: An integral perspective, Phys. Rev. A 91 (2015) 023805.

[19] A. Lubk, A. Béché, J. Verbeeck, Electron Microscopy of Probability Currents at Atomic Resolution, Phys. Rev. Lett. 115 (2015) 176101.

[20] T. J. Pennycook, A. R. Lupini, H. Yang, M. F. Murfitt, L. Jones, P. D. Nellist, Efficient phase contrast imaging in STEM using a pixelated detector. Part I: Experimental demonstration at atomic resolution, Ultramicroscopy 151 (2015) 160–167.

[21] H. Yang, T. J. Pennycook, P. D. Nellist, Efficient phase contrast imaging in STEM using a pixelated detector. Part II: Optimisation of imaging conditions, Ultramicroscopy 151 (2015) 232–239.

[22] K. Müller, F. F. Krause, A. Beche, M. Schowalter, V. Galioit, S. Löffler, J. Verbeeck, J. Zweck, P. Schattschneider, A. Rosenauer, Atomic electric fields revealed by a quantum mechanical approach to electron picodiffraction, Nature Communications 5 (2014) 56531–8.

[23] P. Ehrenfest, Bemerkung über die angenäherte Gültigkeit der klassischen Mechanik innerhalb der Quantenmechanik, Zeitschrift für Physik 45 (1927) 455–457.

[24] E. M. Waddell, J. N. Chapman, Linear imaging of strong phase objects using asymmetrical detectors in STEM, Optik 54 (1979) 83–96.

[25] J. C. H. Spence, J. M. Zuo, Large dynamic range, parallel detection system for electron diffraction and imaging 59 (1988) 2102–2105.

[26] K. Müller, H. Ryll, I. Ordavo, S. Ihle, L. Strüder, K. Volz, J. Zweck, H. Soltau, A. Rosenauer, Scanning transmission electron microscopy strain measurement from millisecond frames of a direct electron charge coupled device, Appl. Phys. Lett. 101 (2012) 212110.

[27] V. B. Ozdol, C. Gammer, X. G. Jin, P. Ercius, C. Ophus, J. Ciston, A. M. Minor, Strain mapping at nanometer resolution us-

ing advanced nano-beam electron diffraction, Applied Physics Letters 106 (2015) 253107.

[28] K. Müller-Caspary, A. Oelsner, P. Potapov, Two-dimensional strain mapping in semiconductors by nano-beam electron diffraction employing a delay-line detector, Applied Physics Letters 107 (2015) 072110.

[29] R. Turchetta, J. Berst, B. Casadei, G. Claus, C. Colledani, W. Dulinski, Y. Hu, D. Husson, J. L. Normand, J. Riester, G. Deptuch, U. Goerlach, S. Higueret, M. Winter, A monolithic active pixel sensor for charged particle tracking and imaging using standard {VLSI} {CMOS} technology, Nuclear Instruments and Methods in Physics Research Section A: Accelerators, Spectrometers, Detectors and Associated Equipment 458 (2001) 677–689.

[30] A.-C. Milazzo, P. Leblanc, F. Duttweiler, L. Jin, J. C. Bouwer, S. Peltier, M. Ellisman, F. Bieser, H. S. Matis, H. Wieman, P. Denes, S. Kleinfelder, N.-H. Xuong, Active pixel sensor array as a detector for electron microscopy, Ultramicroscopy 104 (2005) 152–159.

[31] A. Rosenauer, M. Schowalter, STEMsim - A new software tool for simulation of STEM HAADF Z-contrast imaging, in: A. G. Cullis, P. A. Midgley (Eds.), Springer Proceedings in Physics, volume 120, Springer, 2007, pp. 169–172.

[32] B. A. Lippmann, Ehrenfest's Theorem and Scattering Theory, Phys. Rev. Lett. 15 (1965) 11–14.

[33] R. Erni, M. D. Rossell, C. Kisielowski, U. Dahmen, Atomic-Resolution Imaging with a Sub-50-pm Electron Probe, Phys. Rev. Lett. 102 (2009) 096101.

[34] H. Sawada, Y. Tanishiro, N. Ohashi, T. Tomita, F. Hosokawa, T. Kaneyama, Y. Kondo, K. Takayanagi, STEM imaging of 47-pm-separated atomic columns by a spherical aberration-corrected electron microscope with a 300-kV cold field emission gun, Journal of Electron Microscopy 58 (2009) 357–361.

[35] C. Mahr, K. Müller-Caspary, T. Grieb, M. Schowalter, T. Mehrtens, F. F. Krause, D. Zillmann, A. Rosenauer, Theoretical study of precision and accuracy of strain analysis by nano-beam electron diffraction, Ultramicroscopy 158 (2015) 38–48.

[36] P. Geuens, D. V. Dyck, The S-state model: a work horse for HRTEM, Ultramicroscopy 93 (2002) 179–198.

[37] J. Broeckx, M. O. de Beeck, D. V. Dyck, A useful approximation of the exit wave function in coherent STEM, Ultramicroscopy 60 (1995) 71–80.

[38] S. Findlay, N. Shibata, H. Sawada, E. Okunishi, Y. Kondo, Y. Ikuhara, Dynamics of annular bright field imaging in scanning transmission electron microscopy, Ultramicroscopy 110 (2010) 903–923.

[39] G. Anstis, D. Cai, D. Cockayne, Limitations on the s-state approach to the interpretation of sub-angstrom resolution electron microscope images and microanalysis, Ultramicroscopy 94 (2003) 309–327.

[40] S. Findlay, N. Shibata, H. Sawada, E. Okunishi, Y. Kondo, T. Yamamoto, Y. Ikuhara, Robust atomic resolution imaging of light elements using scanning transmission electron microscopy, Applied Physics Letters 95 (2009) 191913.

[41] A. Weickenmeier, H. Kohl, Computation of absorptive form factors for high-energy electron diffraction, Acta Crystallogr., Sect. A 47 (1991) 590–597.

[42] K. Kimoto, T. Asaka, X. Yu, T. Nagai, Y. Matsui, K. Ishizuka, Local crystal structure analysis with several picometer precision using scanning transmission electron microscopy, Ultramicroscopy 110 (2010) 778–782.

[43] A. B. Yankovich, B. Berkels, W. Dahmen, W. Binev, S. I. Sanchez, S. A. Bradley, A. Li, I. Szlufarska, P. M. Voyles, Picometre-precision analysis of scanning transmission electron microscopy images of platinum nanocatalysts, Nature Communications 5 (2014) 4155.

[44] D. Van Dyck, Is the frozen phonon model adequate to describe inelastic phonon scattering?, Ultramicroscopy 109 (2009) 677–682.

[45] A. Rosenauer, M. Schowalter, J. T. Titantah, D. Lamoen, An emission-potential multislice approximation to simulate thermal diffuse scattering in high-resolution transmission electron microscopy, Ultramicroscopy 108 (2008) 1504–1513.

[46] Z. L. Wang, The 'Frozen-Lattice' Approach for Incoherent Phonon Excitation in Electron Scattering. How Accurate Is It?, Acta Crystallogr., Sect. A 54 (1998) 460–467.

[47] R. F. Egerton, Electron Energy-Loss Spectroscopy in the Electron Microscope, 2nd ed., Plenum Press, New York, 1996.

[48] P. E. Batson, J. Silcox, Experimental energy-loss function, $Im[-\frac{1}{\epsilon}(q,\omega)]$, for aluminum, Phys. Rev. B 27 (1983) 5224–5239.

[49] D. B. Williams, C. B. Carter, Transmission electron microscopy, Plenum Press, New York, 1996.

[50] S. Löffler, I. Ennen, M. Stöger-Pollach, P. Schattschneider, Towards orbital mapping in the TEM — Non-Lorentzian angular dependence in core losses, in: Proceedings of the Microscopy Conference 2011, volume 1, DGE — German Society for Electron Microscopy e.V. Germany, Kiel, Germany, 2011.

[51] S. Löffler, Study of real space wave functions with electron energy loss spectrometry, Ph.D. thesis, Vienna University of Technology, 2013. URL: http://permalink.obvsg.at/AC11224780.

[52] S. Löffler, M. Bugnet, N. Gauquelin, S. Lazar, E. Assmann, K. Held, G. A. Botton, P. Schattschneider, Real-space mapping of electronic orbitals, 2015.

[53] P. Blaha, K. Schwarz, J. L. G. K. H. Madsen, D. Kvasnicka, Wien2k, An Augmented Plane Wave + Local Orbitals Program for calculating crystal properties, ISBN 3-9501031-1-2, Technische Universität Wien, Austria, 2001.

[54] P. Schattschneider, M. Nelhiebel, H. Souchay, B. Jouffrey, The physical significance of the mixed dynamic form factor, Micron 31 (2000) 333–345.

[55] S. Löffler, V. Motsch, P. Schattschneider, A pure state decomposition approach of the mixed dynamic form factor for mapping atomic orbitals, Ultramicroscopy 131 (2013) 39 – 45.

[56] E. J. Kirkland, Advanced computing in electron microscopy, Plenum Press, 1998.

[57] F. F. Krause, M. Schowalter, T. Grieb, K. Müller-Caspary, T. Mehrtens, A. Rosenauer, Effects of instrument imperfections on quantitative scanning transmission electron microscopy, Ultramicroscopy 161 (2016) 146–160.

[58] L. Jones, P. D. Nellist, Identifying and Correcting Scan Noise and Drift in the Scanning Transmission Electron Microscope, Microscopy and Microanalysis 19 (2013) 1050–1060.

[59] P. D. Nellist, Electron microscopy: Atomic resolution comes into phase, Nature Physics 8 (2012) 586–587.

[60] N. Shibata, Y. Kohno, S. D. Findlay, H. Sawada, Y. Kondo, Y. Ikuhara, New area detector for atomic-resolution scanning transmission electron microscopy, Journal of Electron Microscopy 59 (2010) 473–479.

[61] J. Chapman, I. McFadyen, S. McVitie, Modified differential phase contrast Lorentz microscopy for improved imaging of magnetic structures, Magnetics, IEEE Transactions on 26 (1990) 1506–1511.

[62] J. Zweck, T. Zimmermann, T. Schuhrke, TEM imaging and evalution of magnetic structures in Co/Cu multilayers, Ultramicroscopy 67 (1997) 153–162.

[63] L. Strüder, H. Bräuninger, U. Briel, R. Hartmann, G. Hartner, D. Hauff, N. Krause, B. Maier, N. Meidinger, E. Pfeffermann, M. Popp, C. Reppin, R. Richter, D. Stötter, J. Trümper, U. Weber, P. Holl, J. Kemmer, H. Soltau, A. Viehl, C. Zanthier, A 36 cm² large monolythic pn-charge coupled device x-ray detector for the European XMM satellite mission, Rev. Sci. Instrum. 68 (1997) 4271–4274.

[64] V. Migunov, H. Ryll, X. Zhuge, M. Simson, L. Strüder, K. J. Batenburg, L. Houben, R. E. Dunin-Borkowski, Rapid low dose electron tomography using a direct electron detection camera, Scientific Reports 5 (2015) 14516.

[65] C. Gammer, V. B. Ozdol, C. H. Liebscher, A. M. Minor, Diffraction contrast imaging using virtual apertures, Ultramicroscopy 155 (2015) 1–10.

[66] M. W. Tate, P. Purohit, D. Chamberlain, K. X. Nguyen, R. Hov-

den, C. S. Chang, P. Deb, E. Turgut, J. T. Heron, D. G. Schlom, D. C. Ralph, G. D. Fuchs, K. S. Shanks, H. T. Philipp, D. A. Muller, S. M. Gruner, High Dynamic Range Pixel Array Detector for Scanning Transmission Electron Microscopy, Microscopy and Microanalysis FirstView (2016) 1–13.

[67] P. Goodman, G. Lehmpfuhl, Observation of the breakdown of Friedel's law in electron diffraction and symmetry determination from zero-layer interactions, Acta Crystallographica Section A 24 (1968) 339–347.

[68] K. Müller, A. Rosenauer, M. Schowalter, J. Zweck, R. Fritz, K. Volz, Strain measurement in semiconductor heterostructures by scanning transmission electron microscopy, Microsc. Microanal. 18 (2012) 995–1009.